ERDA

Progress Report :
Radioisotope Studies Utilizing a Low Level Whole Body Counter
and
Clinical Applications of Activation Analysis

April 30, 1975

Principal Investigator

A.B. Brill, M.D., Ph.D.

NOTICE

This report was prepared as an account of work sponsored by the United States Government. Neither the United States nor the United States Energy Research and Development Administration, nor any of their employees, nor any of their contractors, subcontractors, or their employees, makes any warranty, express or implied, or assumes any legal liability or responsibility for the accuracy, completeness or usefulness of any information, apparatus, product or process disclosed, or represents that its use would not infringe privately owned rights.

MASTER

Vanderbilt University
Nashville, Tennessee

2869

DISTRIBUTION OF THIS DOCUMENT IS UNLIMITED

MAY 1975

PROGRESS REPORT

TABLE OF CONTENTS

Page

A. Dosimetry and Tracer Kinetics 1
1. Methodology 1
a. Hardware Development 1
1. Whole-body Scanning Bed 1
2. CAMAC: Design of an Autonomous Crate Controller . 4
3. Integrated Anger Camera-Stationary Scintillation Probe 5
b. Software Development 7
1. Simulation and Modelling 7
2. Multi-instrument Executive for Data Collection and Display 8
3. Sharing of Computer Programs in Nuclear Medicine. 9
c. Correlation Studies between Calculated and TLD Measurements of radiation dose - applied to Tc-99m Sulfur Colloid Liver Scanning 10
d. Positron Time-of-Flight Imaging System - feasibility study 20
2. Specific Projects 22
a. Dosimetry of New Tc-99m labelled Lung Scanning Agents in Abnormals 22
b. Fe-59 Dosimetry - Abnormals 28
c. Dosimetry of I-131 Hippuran in Bi-lateral and Transplant Renograms 32
d. Dosimetry of Tc-99m labelled Pyrophosphates 37
e. Neutron Dosimetry from Fluorescent Thyroid Scanning . 39
f. Integration of Ultrasound with Scintillation Images . 40
g. Solid State Dosimetry..... 44
B. Clinical Applications of Activation Analysis 50
1. Measurement of Deuterium and Deuterium-Labelled Compounds using the (γ,n) Reaction 50
2. Cf-252 Neutron Activation Facility - feasibility study .. 52
C. Appendix I: The Linear Pan Correction..... 55
Appendix II: The Method of Activity Determination in Patients. 58
Appendix III: Publications..... 71

A. Dosimetry and Tracer Kinetics
1. Methodology
a. Hardware Development
1. Whole-body Scanning Bed

The collection of data required for extensive dosimetry investigations and surveys from routine clinical patients is complicated by the time and inconvenience involved in repeated measurements on often very ill people. In order to increase the number of patients with various forms of pathology in whom we are able to assay the isotopic distribution we have designed and begun the implementation of a computer controlled scanning bed/scintillation camera data collection system. Figure shows a block diagram of the system. This data collection system was developed around a CAMAC module crate interfaced to the PDP/9 computer (ref. 1974 AEC Report). The scanning bed allows the effective field of view of the scintillation camera to be increased to that requried for a total body image. The scanning bed system consists of two parts, i.e., bed control and camera data acquisition. The camera data acquisition system consists of the standard scintillation camera, a commercial ADC for digitization of the position signals and a CAMAC input register module. The ADC is designed to allow the collection of images using two photopeak energies. The image information is transferred from the input register into the computer by program control. While this is slower than direct memory access count rates observed in clinical studies (~1000cps) can be collected with less than 3% data loss. The bed control subsystem consists of a CAMAC output register module and an in-house designed module containing line drivers, status register and level converter. The bed can be scanned with a positional accuracy of .01 inch. The computer can control the direction and motion of the bed but the scanning speed is determined by the motor controller on the bed. The maximum scan size is approximately 75 inches by 30 inches and requires a minimum of 10 minutes for a 4 line 75 inch scan. During collection of a whole body image the bed with the patient is scanned along the length of the bed. When the end of the scan line is reached the bed indexes side ways 6 inches and returns along the length of the bed.

Data from the camera is combined with that indicating the bed position and stored in list mode on either disc or magnetic tape. This data format allows the reconstruction of the image or any subsection of the image with high digital resolution. All image data are stored with a resolution of 256 x 256 which is more than adequate for the scintillation camera.

Figure 2 shows the anterior and posterior views of a Tc-99m polyphosphate whole body scan acquired with this system. Each view consists of 3 scan lines separated by 8 inches. Each of the 65 inch scan lines required approximately 5 minutes to collect for a total of 15 minutes per view. The image reconstruction and photo generation also requires approximately 10 minutes per view. Thus a total time of 50 minutes is requried for this study. This is compared to the 1½ to 2½ hours required for a comparable study performed with the rectilinear whole body scanner. These images each contain about 300 K counts and are comparable in information content to those obtained from the scanners. The images shown here are in a 128 x 500 digital array. It is possible to rebuild subregions of the image with higher digital resolution thus providing a "close up" view of any region of interest. The images may also be manipulated by a software package we developed to provide contouring; smoothing, and foreground-background erase. It should be noted that the computer controls the scanning process and thus allows one to scan any smaller region than the entire body if one wishes and consequently not spend time imaging body reigons not of interest to the current study.

The dual isotope capability of the camera acquisition subsystem can be used with the scanning bed to allow us to do dual isotope imaging. In this case however the 256 x 256 resolution is degraded to 128 x 256 to allow one data bit to be used as an isotope flag for image reconstruction.

The scanning bed imaging system will be used in the investigation of the dosimetry of Tc-99m labelled pyrophosphates. This radiopharmaceutical is rapidly gaining popularity for clinical whole body bone imaging but as yet there has been little quantitative dosimetry performed. The scanning bed will allow us to obtain data on the distribution of Tc-labelled pyrophosphates (and related compounds used in our clinic) in a large number of patient studies. In this instance the scanning bed has several advantages over the dual probe whole body scanner. These are:

1. decreased scanning time
2. the response of the camera is more depth independent than the focused collimaters of the scanner
3. finer digital detail is available.

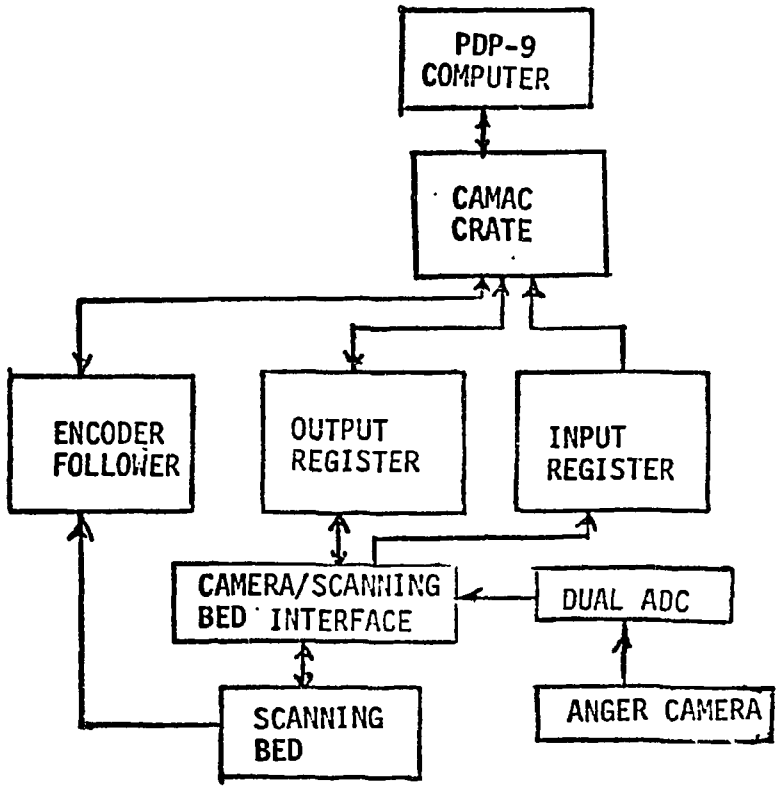

Figure 1 Block diagram of Scanning Bed Data Acquisition System.

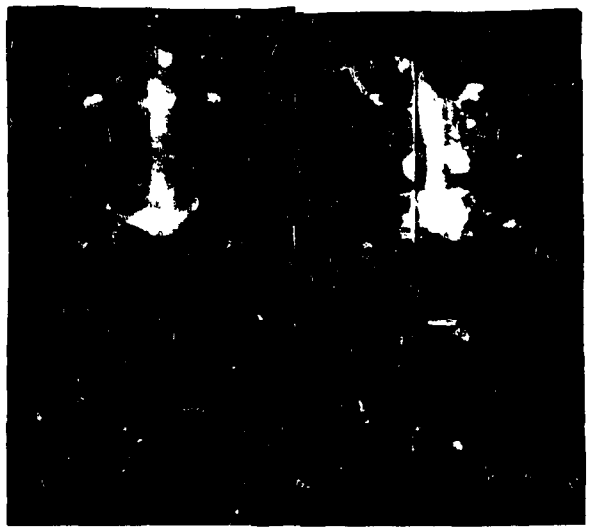

ANTERIOR POSTERIOR

Figure 2 Whole Body Scans of Patient collected with Scanning Bed.

2. CAMAC: Design of an Autonomous Crate Controller

Experience with the CAMAC instrumentation system continues to demonstrate to us that such standardization and modularity benefit medical systems by enabling them to become operational sooner and to be both more reliable and more easily repaired than those containing special purpose electronics. CAMAC is supported by a crate which conforms to AEC specification TID-25875. This crate is connected to one of the PDP-9 computers by means of a dedicated controller adapted from an Argonne National Laboratories design.

Funds were requested by not granted last year to bring this system into conformity with AEC specification TID-25876. The reasons for this request remains with us:

1. In developing new diagnostic techniques, such as scanning bed tomography, multiple energy camera studies, etc. it becomes necessary to test new devices and concepts without jeopardizing operational systems.
2. Higher data rates are rapidly saturating the capacity of our home-made controller.
3. The need to share results with other medical users of CAMAC, such as the Meson production facility at Los Alamos, suggests a level of standardization which is independent of the computer used. The addition of a second PDP-9 computer has provided its own pressure for a parallel CAMAC system, both for back-up and through-put.

In the absence of funds, CAMAC components were borrowed from the experimental inventory at Fermi National Accelerator Laboratories to test specific concepts before the CAMAC hardware was returned to Fermi. We remained in contact with the several national laboratories using CAMAC and participated in the review of a Fermi-designed autonomous crate controller, which is comparable in price but promises to be higher in performance than a full-blown TID-25876 branch highway CAMAC system. Test results are anticipated by the end of June.

3. Integrated Anger Camera-Stationary Scintillation

We are currently investigating the utility of data collected from the same subject simultaneously, by an Anger Camera and stationary probes. This technique will be used to collect data in studies where the Anger Camera alone yields inadequate data for analysis. These include liver, lung, and renal function studies where the field of view of the camera is inadequate to capture all of the pertinent regions of interest. Data presented in the section on I-131 Hippuran dosimetry demonstrates the potential utility of the collection system. In these studies, the camera is capable of monitoring the kidneys but frequently the bladder is not visualized. Typically, the camera provides marginal data on the blood pool clearance. The addition of a two probe system would yield data on all of these regions of interest simultaneously. In our present configuration the camera data are collected off-line in an Intertechnique cine-scintigraphy system while the probe data are collected directly into the PDP-9 via CAMAC modules.

A block diagram of the integrated camera/probe data acquisition system is shown in Figure 1. Figure 2 shows an example of the data obtained from the integrated system from a patient receiving a renogram at day 10 post-transplantation.

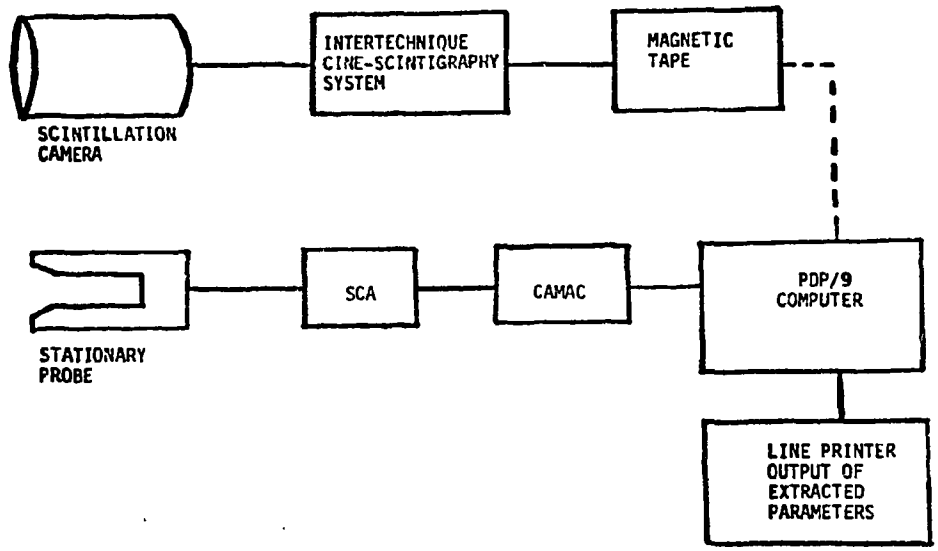

Figure 1. Schematic of Combined Scintillation Camera Stationary Probe Data Collection System

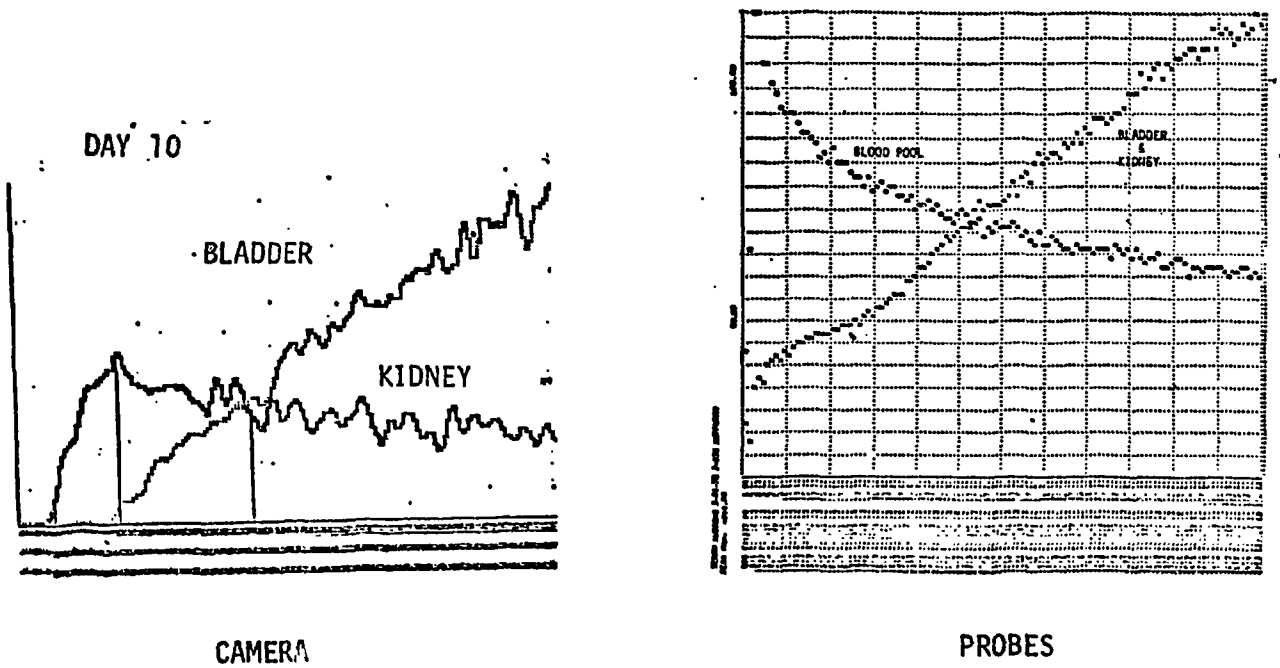

Figure 2. Combined Camera/Probe Renogram Study

b. Software Development
   1. Simulation and Modelling

We are continuing to develop and test new kinetic models in an effort to understand better the total body and organ retention of medically administered radioactive materials. Solutions to these models have been sought generally through the use of Berman's SAAM 25 computer program. Our efforts are being directed toward improving model accuracy through the use of external quantitative measurements as supplemental to routine kinetic data. Models are currently being used to analyze data from studies of iron, I-131 hippuran, pyrophosphate and iodine kinetics in addition to a number of new radippharmaceuticals. The details of these models and model calculations will be discussed in the following sections dealing with the specific material.

2. Multi-instrument Executive for Data Collection

The executive for operating multiple instruments concurrently and asynchronously received routine use and was also extended in capability. This is important to our research since, for instance, routine use of the low level counting facility with the computer, places a relatively low average data rate burden upon the PDP-9 computer yet requires rapid response from the computer to control the position of the scanner without introducing positional skew due to dead time. Similar situations occur with other devices, whether the data acquisition and display instruments are interfaced through the AEC standard CAMAC system or through dedicated pre-CAMAC hardware.

Presently running under the "Background-Foreground Monitor" (supplied by Digital Equipment Corporation), this substantial program (the executive is over 4500 lines of source code, much of this in "macro instruction") permits the simultaneous utilization of the following devices:

1. The low level whole body counting facility in a rectilinear scanning mode.
2. The electrical storage tube video buffer for local and remote graphic and image display.
3. A multichannel analyzer in a frame mode of image acquisition.
4. Via CAMAC:
   a. Position encoders for two independent and autonomous rectilinear scanners.
   b. Event sensors from remote locations, such as QRS-complex discriminator or beginning-of-procedure indications from the Cardiac Cathetherization Facility.
   c. Multiple scaler/counter units which capture physiological information from the patient under study.
5. Transfers of cinescintigraphy system to:
   a. Industry standard magnetic tape (available on one PDP-9).
   b. Proprietary DEC tape which is available on both PDP-9s.
   c. Directly to the second PDP-9.

The PDP-9 system upon which the executive was first made operational was expanded to include 1 million words of head-per-track disk. Suitable modifications were made in executive so that this high-speed medium is now the primary data collection buffer, with the slower DEC tapes serving to record the data without the pressure of real-time acquisition.

The executive program is very modular in architecture so as to facilitate new requirements. Extensive use is made of the CAMAC macro instructions to enhance the initial programming task, to guard against obsolescence, and to promote the sharing of technology. It is anticipated that additional data acquisition and display capabilities can be added readily. Documentation of the executive is complete and reports on these systems will be presented annually to the Oak Ridge Symposia on the Sharing of Computer Technology in Nuclear Medicine.

3. The Sharing of Computer Programs in Nuclear Medicine

During the past year we have received and distributed numerous computer programs for the quantitation and analysis of radioisotopic spectral and image data. We have continued to work with Dr. Berman and Mrs. Weiss to help distribute the NIH Simulation and Modelling Program package (SAAM) to users with 32-bit computers. During the past year we have supplied copies to two medical centers (University of Wisconsin-Milwaukee and the Orange County Medical Center - California). We will continue to help introduce new users to the capabilities of the SAAM programs for the analyses of kinetic data and the calculation of radiation absorbed doses.

Recently we have received a program called CAMIRD (Computer Assisted Medical Internal Radiation Dosimetry) from the Cincinnati General Hospital. CAMIRD computes absorbed doses to specified organs in a standard man from internally administered radionuclides according to the MIRD schema. We are in the process of implementing this program on our Sigma-7 computer to aid us in our continuing dosimetry calculations.

As part of our continuing effort to promote the sharing of computers programs in nuclear medicine, we co-sponsored the Fifth Annual Symposium on the Sharing of Computer Programs and Technology in Nuclear Medicine. The symposium was held January 15-17, 1975 in Salt Lake City, Utah and resulted in the formation of a number of a number task groups assigned to investigate significant problems in the analysis of radioisotopic data. We continue to take an active part in the standardization of computer technology (both hardware and software) in nuclear medicine.

c. Correlation Studies between Calculated and TLD Measurements of Radiation Dose - Applied to Tc-99m Sulfur Colloid Liver Scanning

The position average dose D to a target region due to a source of activity A(t) can be calculated from

$$D = \int_{t_1}^{t_2} A(t)\ mCi \cdot k\ \frac{photons}{mCi \cdot sec} \cdot R\ \frac{rads}{photon} \cdot dt\ sec \tag{1}$$

or

$$D = k\,R \int_{t_1}^{t_2} A(t)\,dt\,,$$

where t_1 and t_2 define the time interval over which the dose is computed. This equation is equivalent to the formalism given in MIRD Pamphlet #1, but is more convenient to use because the quantity R is computed for a given radionuclide and source-target pair, whereas absorbed fractions are computed only for individual radiation energies. The purpose of this project is to measure the dose D and activity A(t) in patients, and check for agreement between this measured dose and that calculated from (1) using the value of R computed from the standard man model of Snyder, et. al.[1] Thus we are making an evaluation of our methods of dose and activity measurement, as well as the applicability of the standard man model for internal dosimetry calculations.

For this, we are using male patients who have received Tc-99m sulfur colloid liver scans. The source organs are the liver and spleen, and the target region is a 2" x 2" x 0.035" thick slab of LiF on the patient's skin, anterior to and directly overlaying the liver. The dose measurements are made with LiF TLD's, the activity measurements are made with the Vanderbilt University Low-Level Counter, and R has been calculated by Dr. J.W. Poston and his associates at ORNL.

In a study of this type, it is very important that the accuracy with which D and A can be measured is known. The precision of TLD measurements has already been discussed, so this section will concentrate mainly on the accuracy of activity measurements. At the end, some patient data will be given.

The method of activity determination initially planned was that reported by Watts.[2] We have previously discovered and reported[3,4] that this method does not take self-attenuation by the source into account; our efforts this past year have been in analyzing the effects of the x-y distribution of patient activity (depth = z distribution) on our activity estimates, since variable attenuation effects would be present here also. Because the collimator field of view is larger than the scan cell size, it is not clear what these effects are. In Watts' method, one is forced to assume that these effects are the same for both calibration scans ("point" sources in constant thickness water phantoms) and patient scans (distributed

sources in the variable body thickness), which might not be true. In addition, the geometric mean (GM) of the top and bottom detector responses is used to calculate the activity estimate, but it is not clear whether one should compute a GM point-by-point and sum these GMs over the scan image to get the total source activity, or first sum the detector responses over the image and compute the GM of these sums. In general, these two methods of data handling will not give the same results (i.e., GM of sums $\neq$ sum of GMs).

The investigation of these questions has been primarily mathematical, although some experimental evaluation using patient data has been done. The mathematical details are given in Appendix II. In this section, emphasis will be given to the assumptions used and conclusions reached reached from the contents of Appendix II.

In order to set up the formalism, imagine the scan field to be divided up into a large number of rectangles, or cells, as shown in Figure 1. The length of each cell is equal to the distance moved by the scanner when counts are recorded for one data point, and the width of each cell is equal to the distance between scan lines. When the detectors traverse the length of a cell, the counts accumulated in that time are recorded by a computer, thus giving a data point corresponding to that cell.

To calibrate the scanner, a "point" source of known activity is placed in a constant thickness phantom and scanned. We define

$$S_{ij}(d,z) = \frac{\text{counts recorded in data point } i \text{ due to the source in cell } j}{\text{source activity}} \quad (2)$$

where d is the phantom thickness and z the height of the source from the bed. In order that this be a well-defined parameter, one must have the cell sizes much smaller than the area of the collimator field of view. Otherwise, the precise x-y location of the "point" source within a given cell would be important.

There would be a calibration factor of the form of (2) for each detector. To obtain a useful calibration function, one has two choices. Either sum the factors for each detector over the entire image and take the geometric mean of these sums, or else find the geometric mean point-by-point over the image, and add up these geometric means. The former is preferred, because it is more nearly independent of z than the latter, especially if the value of z is such that the collimator fields of view of the two detectors have unequal areas. (This is due to the fact that if <u>either</u> top or bottom S_{ij} is zero, then the latter method gives a zero contribution to the calibration function. For the former, <u>both</u> top and bottom S_{ij} must be zero to do this.) Also, the major reason for using the geometric mean is to get a calibration function that is nearly independent of z.

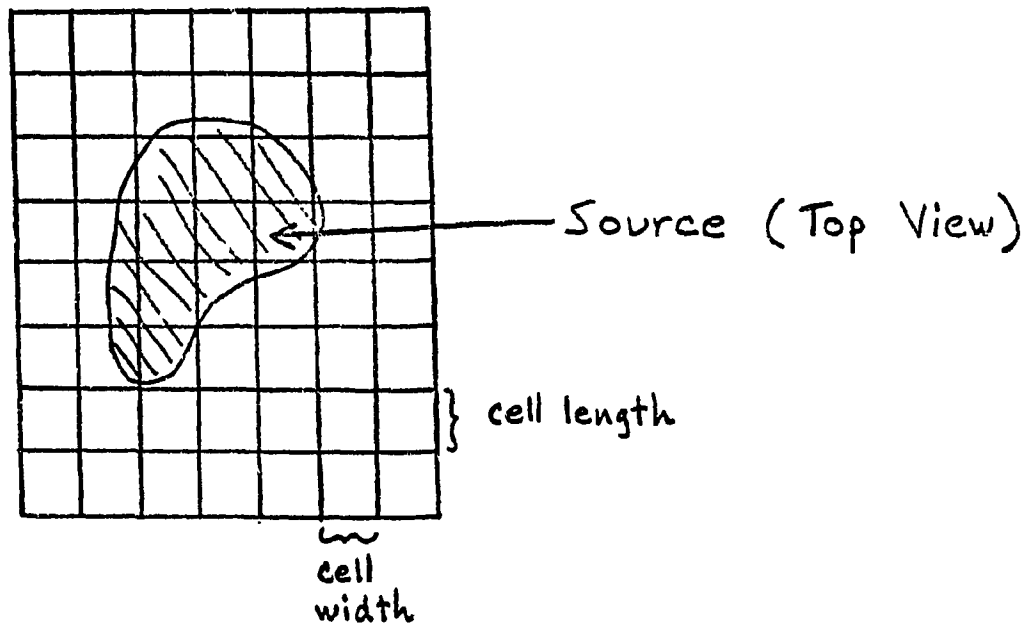

Figure 1. The division of the scan field. The size of the cells is greatly exaggerated for clarity. In this case, there are 56 cells in the scan field. In the usual case, there are 4096.

For a patient scan, the patient thickness changes from one cell to another, as does the source thickness. The source thickness variation causes little problem because the source can be viewed, to a good approximation, as a series of adjacent cells each of which contains a constant thickness source, which we know how to take into account.[4] But the variable patient thickness causes substantial problems. To begin with, the calibration scan was done in a constant thickness phantom. So when one tries to write the detector counts from the patient scan in terms of S_{ij}, it is unclear what patient thickness value should be used. Next, one must sum over the patient image before taking the geometric mean of the detector counts in order to be able to write the detector counts in terms of the calibration function. This geometric mean is then divided by the calibration geometric mean for some sort of average patient thickness, which remains to be determined. Then, even if one gets around these obstacles, the resulting expression is too complicated to evaluate directly, because it contains products of terms involving the source thickness and patient thickness for each cell. Since these thicknesses were obtained with different instruments (source thickness from ultrasonic scans and patient thickness from transmission scans), they are not correlated, and accurate correlation is difficult to do. An approximate method of calculation is developed which removes the need for this correlation, but which introduces a geometric condition on the relation

between the source shape and the patient shape. The interpretation of this condition leads to the conclusion that the patient geometry must show some symmetry (but not too much), which probably would not occur for all patients, and might not even occur for any. Despite these problems, it is shown in Appendix II that, with a reasonable assumption, this geometric condition is adequately met because the validity of the equations is not very sensitive to it. This is further demonstrated with patient data, and applied to three cases. Also, a means of checking the self-consistency of this method is given, so that with one simple (if a computer is used) test using the transmission scan data and calibration data, one can check the validity of the approximate calculation. This method has the further advantage of being somewhat general, so that it could be tried for isotopes other than Tc-99m. If it were going to fail in these cases, the test above would probably show this failure. Another advantage is that the equations explicitly show the effects of variable source and patient thicknesses on the activity estimate, making error analysis easier (repetitive scans are often impractical) and giving a researcher a starting place from which to arrive at his own technique, if all the assumptions here cannot be met.

The reasonable assumption referred to above deserves comment, because if it is not met, most of the material in Appendix II is irrelevant. To see what this assumption is, consider a uniform source of varying thickness in a phantom of varying thickness. The counts in data point i due to the activity in cell j would be given by

$$C_{ij} = (A_j / t_j) \int_{z_{j1}}^{z_{j2}} S_{ij}(?, z_j)\, dz_j , \qquad (3)$$

where

A_j = the activity in cell j

t_j = the source thickness in cell j

z_{j1} = the height of the bottom of the source in cell j from the bed

z_{j2} = the height of the top of the source in cell j from the bed

? = the indication that the pahntom thickness to be used is unknown.

In general, the C_{ij} would depend upon the thicknesses and locations of all the cells in the field of view, because of scattered photons. The assumption is that C_{ij} depends only upon d_j, the phantom thickness in cell j, even if $i \neq j$. This is done, and seems reasonable, because

1. The effects of variable phantom thickness will be less for a phantom whose thickness does not vary by too much from one cell to the next, even though cells far apart may have very different thicknesses. For the human trunk, the thickness does change rapidly along the sides, but much less closer to the midline. Little or no patient activity will be located along the sides, so the effects of these cells should be small.

2. Photons of three types (see Figure 2) will be counted. Type A are unscattered photons emitted vertically to a detector, and are attenuated in the cell with thickness d_j. Type B are small-angle scattered photons and unscattered ones emitted at an angle to the vertical. Since the thickness in adjacent cells is not very different, the attenuation of these photons will be about the same as for type A photons. Type C photons are everything else. If they are unscattered photons emitted at a large angle to the vertical, they can be reduced by proper collimation. If they are large-angle scattered photons, they can be reduced by pulse height discrimination, because of their degraded energy.
3. Each part of the source along a scan line is in the center of the collimator field of view precisely once during a scan, so that types A and B photons are counted from all parts of the source.
4. The form of the calibration functions was observed to be exponential with depth. If only type A photons were counted, this should be the case, with μ equal to the published value of the linear attenuation coefficient. We observed μ to be less than this, indicating that some type B, and probably a few type C photons were counted. If many type C photons had been counted, the exponential attenuation would not have been observed.

The method of activity determination would involve the following steps:
1. Sum each detector counts over the desired organ image, without regard to the various source and phantom thicknesses.

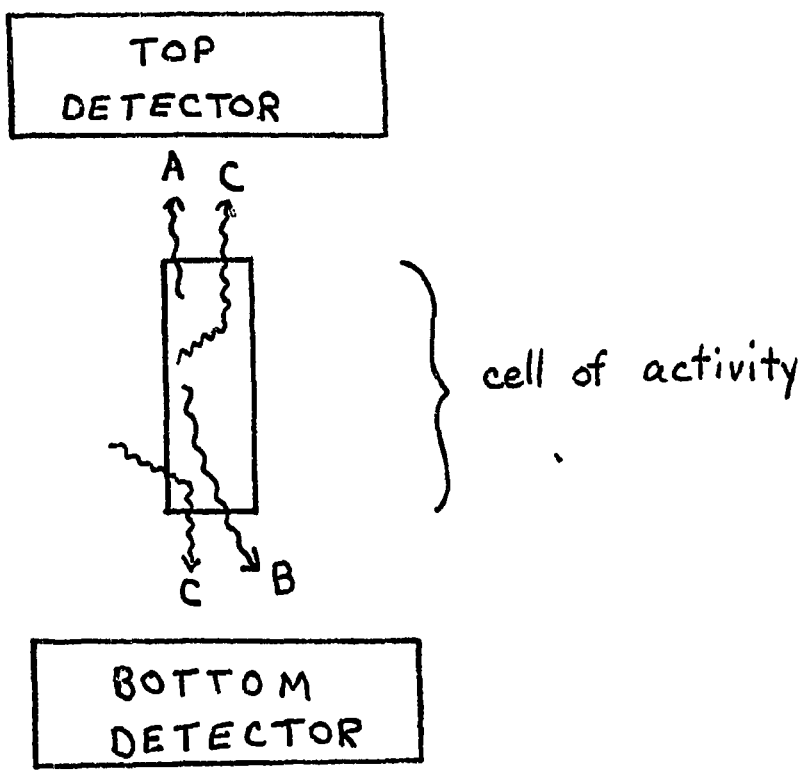

Figure 2. Types A, B, and C photons

If there is more than one source organ in the scan field, only those organs which are resolved can be treated separately. Organs not resolved must be processed as a single source. Naturally, one must subtract background counts from these sums.

2. Using the transmission scan data, compute the average patient thickness (d) from

$$e^{-\mu d/2} = \frac{1}{m} \sum_{j}^{m} e^{-\mu d_j/2},$$

where the d_j are the various patient thicknesses, and m is the number of cells comprising the source. From a knowledge of the number of data points in the image and the size of the collimator field of view, d can be found accurately even if m is not exactly known. Notice that d will be somewhat less than the arithmetic mean of the d_j values; this is important and is discussed in Appendix II.

3. Using the ultrasonic data, evaluate the expression

$$E = \sum_{j}^{m} \sinh(\mu t_j/2) \Big/ \sum_{j}^{m} (\mu t_j/2),$$

where t_j are the various source thicknesses and μ is determined from the exponential attenuation of the calibration data.

4. Calculate the estimate of the source activity from

$$A = (C_T C_B)^{1/2} \Big/ \left[GM(d) \cdot E\right],$$

where

C_T = the sum of the top detector counts

C_B = the sum of the bottom detector counts

E = the expression from step 3

GM(d) = the geometric mean of the calibration functions for each detector. This is assumed to be independent of point source depth, although it does depend upon the phantom thickness.

5. The activity estimate just found will be, at worst, an upper limit to the true source activity, provided that all the terms in the above equation are accurately known. There are three checks which can be run to assume that this upper limit is only negligibly different from the true activity.

a. Check the approximations using the method described in Appendix II with the infinite series.

b. Since the Tc-99m sulfur colloid should be fixed in the liver and spleen, check to see that the activity computed for each organ decays with a six hour half life (this will not uncover systematic errors).

c. Extrapolate the activity estimates back to the time of injection. If the value obtained is somewhat less than the amount withdrawn from the sulfur colloid vial for the patient injection (this number, rather than the amount injected, is recorded for

inventory purposes), then the activity estimate is probably correct. If not, or if they are equal, the activity estimate is probably in error.

Even if all these conditions are met, the activity estimate may still be in error due to systematic errors. Also, some random error might make the above tests difficult to interpret. These errors would include

1. the validity of the assumed thickness dependence on d_j only
2. the accuracy of the assay of the calibration source
3. counting statistics
4. the accuracy with which the calibration functions reflect exponential attenuation
5. whether or not the activity distribution is uniform, as has been assumed throughout
6. a possible error in the way the cell pattern is defined. For the calibration scans, the distance from a given cell to another is a certain number of centimeters. For the patient scan, the distance between these cells is the same number of centimeters, so if the patient is not water-equivalent, this is a different number of mean free paths. An error might result, although the fact that the image is summed over might help minimize it. This possibility needs to be checked using a non-symmetric, heterogeneous phantom, but the patient data taken so far indicates that this is not an important problem.

Two of the patients used in this study were of about the same height and weight as the standard man model used by Dr. Poston, while the third was taller and heavier. For the first two men, the ratio of the dose calculated from equation (1) to that measured with TLD's was 1.7, while for the larger man, it was 2.6. This is a considerable difference, although the calculated dose is larger than the measured (true?) dose. All three of the checks on the activity determination were made and appeared to be adequate. The rate of activity decay implied a half life of slightly less than six hours (> 5.9 hours), the test on the infinite series implied an error of about 1%, and the activity extrapolated back to injection time was about 2.5 mCi. The activity withdrawn from the sulfur colloid vial was 3.0 mCi in each case; the difference of 0.5 mCi may well have been left in the syringe after injection (specific activity of colloid was approximately 10 mCi/ml). This lack of agreement with the doses was disappointing, although the result for the heavier patient shows that the trunk size may be quite important, and could be the cause of the disagreement. Still, it was desired to make a further check of our methodology, using an irregular, but well-defined geometry, if practical. In particular, the photon energies seen by the TLD's on the patients might not be near enough the same as those seen on the cube face, and the activity estimates might be incorrect due to a non-uniform distribution, etc.

A chance to do this occured when Dr. Poston informed us that a physical phantom had been built which closely approximates the mathematical phantom described in MIRD Pamphlet #5. So we did a set of exposures with this phantom at ORNL, using the cube problem to calibrate the TLD's. In addition, a separate exposure was made to account for the fact that different TLD's have different sensitivities, i.e., each TLD was individually calibrated. Two exposures were made at ORNL. In one, a group of thirteen

TLD's was exposed to a known activity in the spleen. In the other, a second group of thirteen TLD's was exposed to a known activity in the liver. With these data, the value of R in (1) could be calculated and compared to the computer calculation, giving the results of Table 2.

Table 2

Results of standard phantom exposure

R as computed from TLD readings(rads/photon)	
Liver	$3.445 \times 10^{-14} \pm 11\%$
Spleen	$2.347 \times 10^{-15} \pm 13\%$
Computer Calculation(rads/photon)	
Liver	$5.305 \times 10^{-14} \pm 12\%$
Spleen	$4.033 \times 10^{-15} \pm 26\%$
Ratio of R Values(Computer/TLD)	
Liver	5.305/3.445 = 1.54
Spleen	4.033/2.347 = 1.72

As can be seen, the computer results were larger than the observed values in this case as well. The uncertainties, which are due mainly to statistics in the Monte Carlo calculations (cube problem and phantom calculations) had to be extended to two standard deviations before the ranges of values overlapped. Further, the ratios of R values are not too different from those observed with patients, suggesting a possible error in the computer calculations. However,we discovered a peculiarity in TLD readings which looks like it might increase the R values, when corrected for.

This peculiarity was noticed when the TLD's were given a known dose of Cs-137 radiation. The sensitivity of the TLD's in this case was found to be 3 counts/mrad, while the cube exposure to Tc-99m gave a sensitivity of 4 counts/mrad. This should not be the case; these sensitivities should be equal. The dose rate from the Cs-137 source has been checked by two independent methods, and appears to be correct. However, the activity of Tc-99m put in the cube was measured with a Squibb Model CRC-6A dose calibrator, and might be in error. The readings of the dose calibrator seem to be consistent (accounting for the earlier verification of the cube problem), but since the activity assays at ORNL were done by ORNL personnel using different equipment, our assays might be inconsistent with theirs, affecting the value of R calculated from TLD readings. We plan to do a cross-check of assays with ORNL to see if this is the case, and make further investigation

with Dr. Poston if better agreement between the TLD measurements and the computer calculations cannot be found. In addition, several more patient studies will be done to better evaluate (1).

References

1. Snyder, W.S., Ford, M.R., Warner, G.G., and Fisher, H.L., Estimates of Absorbed Fractions for Monoenergetic Photon Sources Uniformly Distributes in Various Organs of a Heterogeneous Phantom, Journal of Nuclear Medicine: MIRD Pamphlet #5, supplement #3, 1969.

2. Watts, J.R., Methods for Quantitative Assay of Radioactivity in Man: Total Body and Regional Distributions, Ph.D. Thesis, Vanderbilt University (1971).

3. Radioisotope Studies Utilizing a Low Level Whole Body Counter and Clinical Applications of Activation Analysis, AEC Contract AT-(40-1)-2401, Progress Report, (1974).

4. Jones, J.P., Johnston, R.E., and Brill, A.B., The Validity of an Equivalent Point Source (EPS) Assumption Used in Quantitative Scanning, to be published in Physics in Medicine and Biology.

d. Positron Time-of-Flight Imaging System - feasibility study

We have undertaken, in co-operation with the Nuclear Physics Group of Vanderbilt a feasibility study to determine of current state-of-the-art radiation detection systems make time-of-flight positron imaging a clinical positron annihilate they produce 2 annihilation quanta of approximately 0.511 MeV which by the Principle of the Conservation of Momentum must go in directions at an angle of 180° with respect to one another. Therefore using 2 detectors and coincidence techniques one can determine the line along which the annihilation occurred uniquely. This property has allowed Brownell and several other groups to develop rather complicated positron imaging systems.

If the annihilation does not occur equidistant from the 2 detectors, then the photons will have slightly different arrival times. Light travels in air 30 cm in 10^{-9} sec (1 nano sec). Therefore, if ones detection system is capable of resolving time differentials of a few tenths of a nano second the spacial resolutions will be adequate to do medical imaging of the positron distribution. This technique is referred to as time-of-flight positron imaging.

We have performed a preliminary experiment to determine how accurately we could determine the positron distribution for various source configurations using differential time-of-flight techniques. The experimental set-up is schematically shown in Figure 1.* The incoming quanta are converted to scintillation photons in the plastic (NE 111) scintillator and then converted to an electrical pulse by the Photomultiplier tube. The constant fraction device then relates the pulse to a time measurement and the two times from the two parallel systems are then compared and converted to a voltage in the TAC. This can be displayed on a multichannel analyzer. Each channel then corresponds to a given time differential between the arrival of the two quanta at the detection system. Signals are also taken off the last dynode after amplification and put through a pulse height analyzer. By this energy discriminating one can control the size of accepted pulses seen by a constant fraction device which may then more accurately resolve the timing of the event. One then observes a timing spectrum on the MCA whose position corresponds to the position of the source and of width determined by the time broadening caused by the different components of the detection system. We feel that the equipment we have gathered for this preliminary experiment was true state-of-the-art equipment although we also feel that due to the preliminary nature of what has been done thus far, we should be able to improve our timing spectrum (timing resolution) somewhat.

In order to assess the medical utility of this system, we propose to carry out a number of realistic phantom studies simulating, in particular, lesions of the brain. If the phantom studies prove encouraging, experiments will be carried out in animals with experimentally created lesions.

*The photomultiplier tubes are on loan from RCA; much of the electronics is the property of the Vanderbilt Nuclear Physics Group and the Oak Rige UNISOR Group.

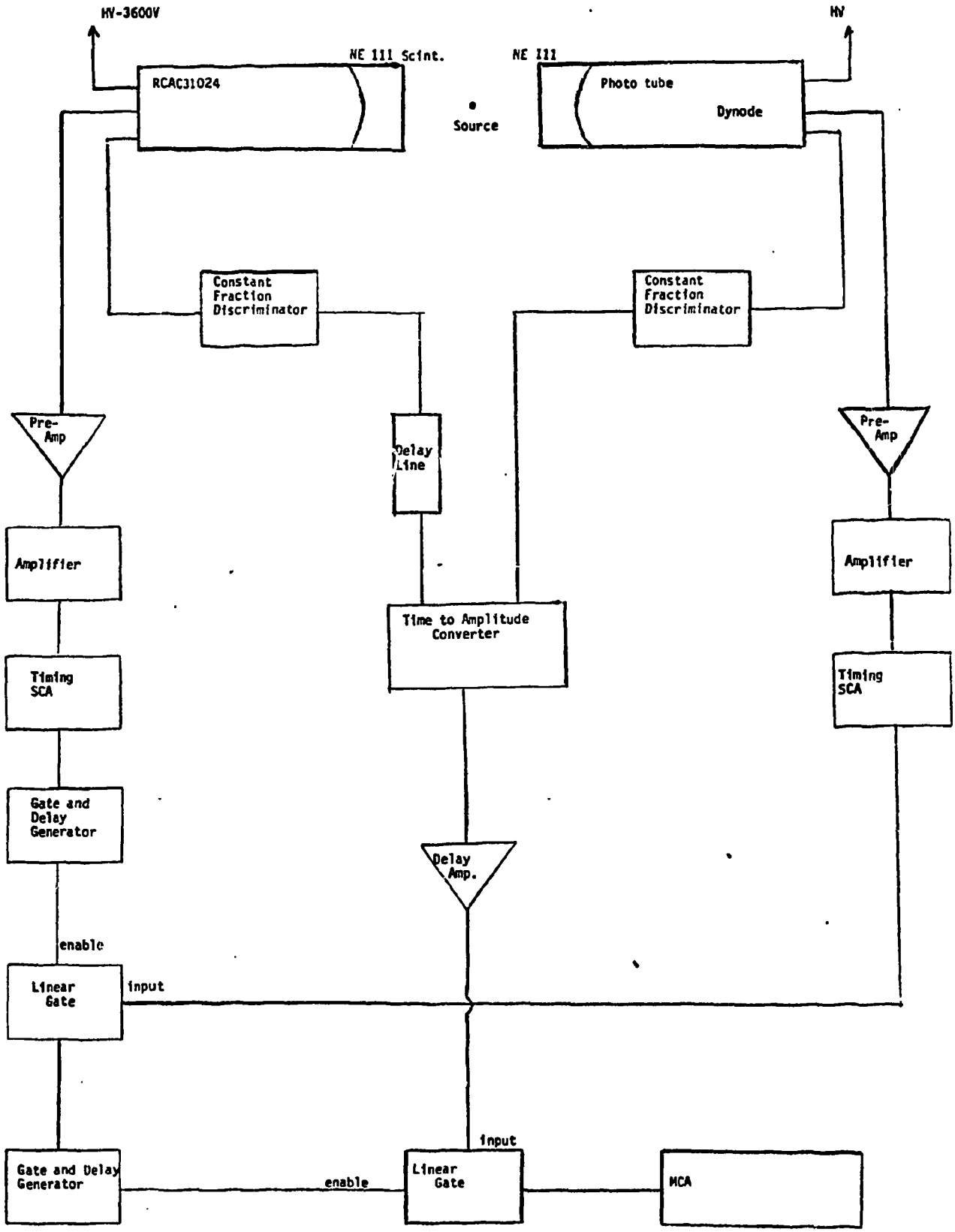

Figure 1. Block Diagram of Positron Time-of-Flight Imaging System

2. Specific Projects
   a. Dosimetry of New Tc-99m labelled Lung Scanning Agents in Abnormals

Results from a pilot study on patients receiving Tc-99m macro-aggregated albumin for lung scans indicated that the biological retention of this material in the lung was much longer than previously had been believed. Since this test is a widely used clinical procedure we decided to determine the radiation dose associated with these studies by collecting quantitative data on biological turnover.

During the last year we carried out studies on 12 normal volunteers. Each volunteer was administered 500 μCi (one-quarter of the recommended dose) of the Tc-99m labelled compounds. Whole body scans and blood samples were taken at 1, 3, 6, and 24 hours post injection. From these data the radiation dose to the total body, lungs and gonads were calculated. During the next year we propose to continue these studies to include a group of approximately 12 abnormal subjects following the same protocol as was used for normal subjects.

Figures 1 and 2 show the averaged biological retention data from the normal studies. Figure 1 is for the group administered the commercially prepared macro-aggregated albumin. The total body and lung retention data are described by the following equations:

Total Body: $$A(t) = 100\, e^{-\frac{0.693t}{52.1}} \quad (r = -0.97)$$

Lungs: $$L(t) = 43.8\, e^{-\frac{0.693t}{4.67}} + 0.50 \quad (r = -0.96)$$

Figure 2 is the data from the group administered the labelled albumin microspheres. The macroaggregate data for both the total-body and lung data show behavior similar to the microsphere date:

Total Body: $$A(t) = 100\, e^{-\frac{0.693t}{48.1}} \quad (r = -0.92)$$

Lungs: $$L(t) = 52.5\, e^{-\frac{0.693t}{3.27}} + 0.40 \quad (r = -0.90)$$

The data shown graphically in Figures 1 and 2 are shown in tabular form in Tables 1 and 2. The errors were calculated based on the spread in the observations. We have made our dosimetry calculations assuming the radioactive source to be uniformly distributed in the lungs obeying the biological retention equations shown above. For the activity not residing in the lungs, we have assumed it to be uniformly distributed in the total body and obeying the following equation:

$$TB(A) = A(t) - L(t),$$

where A(t) is the equation describing the total body activity (including lungs) and L(t) is the lung activity. The cumulative activity A(t) for the total body and lungs for both radiopharmaceuticals are shown in Table 3. Table 4 shows the resulting dose equivalent mCi/day. Tables 5 and 6 show the results of the dose estimates to the total body, lungs, ovaries and testes assuming radiation sources in the lungs and total body.

Upper limits on the self dose to the liver and spleen were estimated assuming each organ to have a 5% uptake (the approximate mean of the observed data) with loss due to radioactive decay only. The estimated doses are as follows:

$\bar{D}_{Liver \quad Liver} \leq$ 19.8 mrem/mCi administerd

$\bar{D}_{Spleen \quad Spleen} \leq$ 143.8 mrem/mCi administered.

The raw data derived from the quantitative whole-body scan are presented in Tables 7 and 8 .

LUNG SCANNING AGENTS
MACROAGGREGATED ALBUMIN

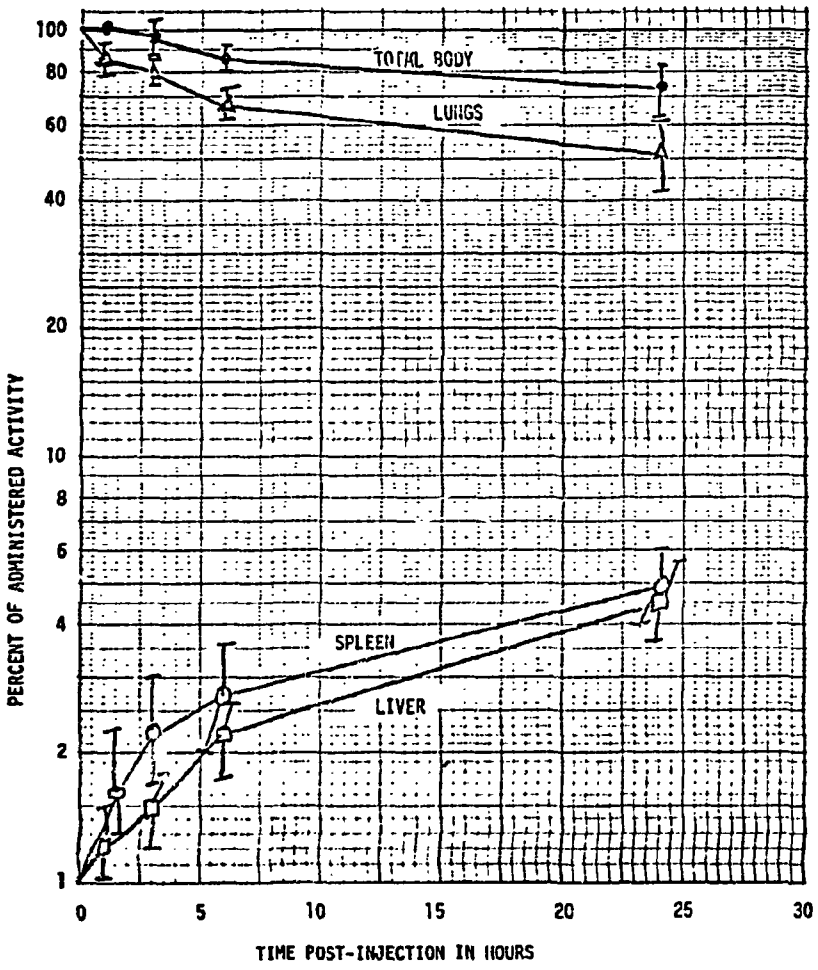

FIGURE 1

LUNG SCANNING AGENTS
ALBUMIN MICROSPHERES

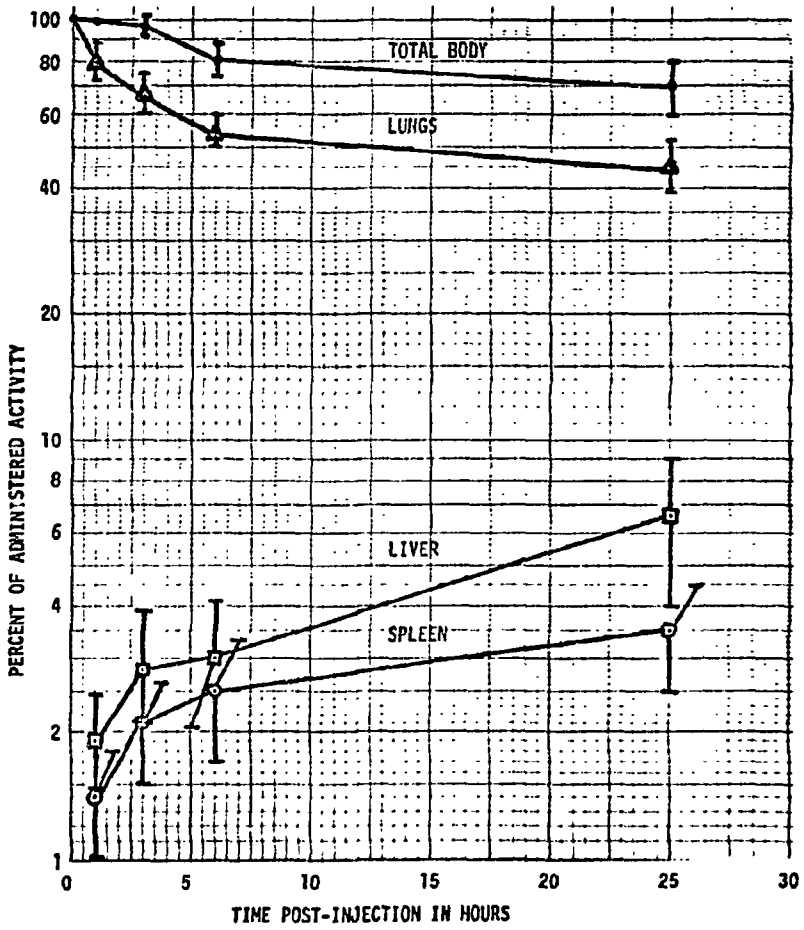

FIGURE 2

Table 1

MACROAGGREGATED ALBUMIN (GROUP MEAN)

Time (hours)	Total Body	Lungs	Liver	Spleen	Blood
.25					2.3 ± 0.6
1	100	86.5 ± 1.3	1.1 ± 0.2	1.6 ± 0.7	5.5 ± 2.6
3	98.1 ± .9	79.6 ± 1.8	1.5 ± 0.2	2.2 ± 0.7	5.2 ± 0.9
6	87.1 ± 2.4	67.5 ± 1.4	2.2 ± 1.4	2.8 ± 0.8	6.5 ± 1.6
24	73.0 ± 14.8	52.3 ± 12.2	4.5 ± 1.2	4.8 ± 1.0	3.2 ± 1.7

Table 2

ALBUMIN MICROSPHERES (GROUP MEAN)

Time (hours)	Total Body	Lungs	Liver	Spleen	Blood
.25					2.3 ± 0.6
1	100	82.3 ± 4.6	1.9 ± 0.4	1.6 ± 0.7	5.5 ± 2.6
3	98.1 ± 0.9	68.5 ± 4.5	2.8 ± 1.0	2.2 ± 0.7	5.2 ± 0.9
6	81.4 ± 6.0	54.7 ± 3.7	3.0 ± 1.0	2.8 ± 0.8	6.5 ± 1.6
24	70.4 ± 12.0	45.1 ± 6.5	6.8 ± 2.9	4.8 ± 1.0	3.2 ± 1.7

Table 3

Cumulative Activity

$$\frac{\text{mCi Days}}{\text{Administered Dose in mCi}}$$

	Total Body	Lungs
Tc-99m Albumin Macroaggregate	0.074	0.248
Tc-99m Albumin Microspheres	0.177	0.169

Table 4

$$\frac{\text{m rem}}{\text{mCi day}}$$

Tc-99m

Target \ Source	Total Body	Lungs
Total Body	46.9	48.5
Lungs	47.0	1260.0
Ovaries	57.2	22.7
Testes	39.8	.019

Table 5

$\frac{\text{m rem}}{\text{mCi Administered}}$

Tc-99m Albumin Macroaggregate

Target \ Source	Total Body	Lungs
Total Body	3.47	12.03
Lungs	3.48	312.48
Ovaries	4.23	5.63
Testes	2.95	.0047

Table 6

$\frac{\text{m rem}}{\text{mCi Administered}}$

Tc-99m Albumin Microspheres

Target \ Source	Total Body	Lungs
Total Body	8.30	8.20
Lungs	8.32	212.94
Ovaries	10.12	3.84
Testes	7.04	.0032

Table 7

ALBUMIN MICROSHPERES
PERCENT OF ADMINISTERED ACTIVITY

Patient	Time (hours)	T. Body	Lungs	Liver	Spleen	Blood
M.S.	.25	100	-	-	-	10.5
	1	100	84.7	2.0	1.0	16.0
	3	92.9	73.6	3.2	1.5	15.9
	6	80.7	59.2	3.1	1.6	14.3
	24	68.2	48.7	7.1	2.7	7.1
M.C.	.25	100	-	-	-	8.51
	1	100	86.3	2.5	1.0	12.25
	3	96.3	70.7	4.0	1.7	14.9
	6	73.4	51.3	4.2	1.9	14.9
	24	71.8	45.3	10.7	4.9	7.6
V.R.	.25	100	-	-	-	9.5
	1	100	76.6	1.7	1.9	12.9
	3	95.0	63.7	2.1	2.9	15.7
	6	87.7	53.2	3.0	3.7	13.8
	24	85.2	50.6	5.5	5.0	8.5
P.C.	.25	100	-	-	-	13.7
	1	100	80.7	1.5	1.7	17.7
	3	91.3	65.8	2.0	2.1	21.5
	6	83.6	55.1	1.8	2.8	19.1
	24	56.3	35.9	4.0	2.6	10.5

Table 8

MACROAGGREGATED ALBUMIN
PERCENT OF ADMINISTERED ACTIVITY

Patient	Time (hours)	T. Body	Lungs	Liver	Spleen	Blood
P.A.	.25	100	-	-	-	2.7
	1	100	87.6	.09	1.0	4.6
	3	97.0	81.4	1.5	1.5	6.0
	6	84.8	68.2	2.0	1.8	7.7
	24	82.5	62.4	3.4	3.6	5.6
B.C	.25	100	-	-	-	2.9
	1	100.0	86.0	1.0	1.3	4.7
	3	99.0	80.7	1.3	1.8	5.2
	6	86.2	67.4	2.1	2.6	7.1
	24	77.7	53.2	4.5	5.8	3.4
J.P.	.25	100	-	-	-	1.9
	1	100	88.2	1.2	1.5	3.5
	2	97.8	77.7	1.7	2.6	5.5
	6	86.7	65.7	2.6	3.7	4.7
	24	50.9	34.9	4.0	4.6	1.8
D.R.	.25	100	-	-	-	1.7
	1	100	84.2	1.3	2.5	9.2
	3	98.4	78.5	1.5	3.0	4.0
	6	90.5	68.8	2.0	3.2	-
	24	80.7	58.5	6.1	5.3	2.1

b. Fe-59 Dosimetry - Abnormals

Recognizing the need for dosimetry data for abnormal subjects, we at Vanderbilt are using our fund of abnormal patients combined with clinical and research instrumentation designed to collect quantitative information to obtain organ retention data by external counting. These studies are very difficult to conduct, especially in very ill patients; however, these data are badly needed and significant effort is devoted to these studies.

The MIRD Committee in the United States is collecting data from laboratories doing dosimetry studies and analyzing the new data along with well-documented literature data. In the past we have supplied the MIRD Committee with extensive data on a number of radiopharmaceuticals and are continuing our relationship. Currently we are a member (R. Price) of the task group charged to collect data on Fe-59 and I-131 iodocholesterol. Data collected at Vanderbilt will be merged with data from the University of California (Donner Laboratory) to create a single data base. The current plan of the task group is to use the Vanderbilt SAAM-25 Iron kinetics model for the calculation of the cumulative organ activity for the compiled data.

The Vanderbilt SAAM-25 model was presented in last years' report. The flow rates and the derived dose estimates for normals and a number of selected abnormals were also presented. A more complete report of the kinetic model parameters are presented in an IAEA publication which is included as an appended document. In cooperation with Dr. Krantz in the Department of Hematology we are continuing to study a variety of patients with various hematologic diseases. We propose to continue these measurements during the next year in order that a more complete sampling of the radiation dose distribution may be obtained. Dose estimates for abnormals have shown large variations from the normal values.

In our calculations we have included the source organs and target organs shown in Table 1. We have taken the blood source distribution to be identical to the total body. In order to calculate the blood self-dose we have ignored the effects of penetrating radiation and assumed the primary dose contribution to be from nonpenetrating radiation. In those studies where measurements were made for periods $\leq$ 45 days, the organ effective half-life was taken to be equal to the physical half-life.

Table 1 was extracted from ORNL Report No. 5000 entitled "A Tabulation of Dose Equivalent per μCi-day for Source and Target Organs of an Adult for Various Radionuclides by W.S. Snyder, et. al.

Table 2 is a summary of our results for a group of abnormals and our average normal. The table is subdivided so that the fractional dose to each target organ from each source organ may be found. The total target dose resulting from all sources is also recorded.

Table 3 contains the list of the working diagnosis of the patients presented in Table 2. In addition the range of these dose estimates are compared to the 1973 report from the Free University of Berlin.

Table 1

Dose Equivalent/Microcurie-day
(rem/μCi-day)

TARGET \ SOURCE	LIVER	SPLEEN	MARROW	TOTAL BODY
LIVER	8.13×10^{-3}	2.13×10^{-4}	2.01×10^{-4}	4.25×10^{-4}
SPLEEN	2.12×10^{-4}	5.77×10^{-2}	2.02×10^{-4}	4.11×10^{-4}
R. MARROW	1.97×10^{-4}	2.15×10^{-4}	4.74×10^{-3}	3.91×10^{-4}
OVARIES	1.73×10^{-4}	1.15×10^{-4}	5.81×10^{-4}	3.98×10^{-4}
TESTES	4.36×10^{-5}	2.42×10^{-5}	6.68×10^{-5}	4.14×10^{-4}
TOTAL BODY	4.13×10^{-4}	4.12×10^{-4}	3.94×10^{-4}	3.66×10^{-4}

Table 2

Radiation Dose in mrad per μCi of

Fe-59 Ferrous Citrate Administered I.V.

SOURCE	TARGET	A(F)	B(F)	C(F)	D(M)	E(M)	F(M)	G(M)	H(F)	I(F)	J(M)	K(M)
Liver	Liver	211.0	106.0	158.0	158.0	132.0	158.0	317.0	370.0	106.0	422.0	53.0
Spleen	"	0.8	1.0	0.6	1.0	0.8	1.0	0.8	0.8	3.0	1.0	0.6
Marrow	"	0.4	0.4	1.0	0.1	0.6	0.9	0.0	0.1	8.0	0.1	1.0
Blood	"	7.0	8.0	22.0	2.0	11.0	17.0	0.6	1.0	6.0	3.0	22.0
Total		219.2	115.4	181.6	161.1	144.4	176.9	318.4	371.9	123.0	426.1	76.6
Liver	Spleen	6.0	3.0	4.0	4.0	3.0	4.0	8.0	10.0	3.0	11.0	1.0
Spleen	"	225.0	299.0	150.0	263.0	225.0	374.0	225.0	225.0	750.0	299.0	150.0
Marrow	"	0.4	0.4	1.0	0.1	0.6	0.9	0.0	0.1	8.0	0.1	1.0
Blood	"	7.0	8.0	21.0	2.0	11.0	16.0	0.5	1.0	5.0	3.0	21.0
Total		238.4	310.4	176.0	269.1	239.6	394.9	233.5	236.1	766.0	313.1	173.0
Liver	Red Marrow	5.0	3.0	4.0	4.0	3.0	4.0	8.0	9.0	3.0	10.0	1.0
Spleen	" "	0.8	1.0	0.6	1.0	0.8	1.0	0.8	0.8	3.0	1.0	0.6
Marrow	" "	9.0	10.0	27.0	3.0	14.0	21.0	0.7	2.0	184.0	3.0	27.0
Blood	" "	6.0	8.0	20.0	2.0	10.0	15.0	0.5	1.0	5.0	3.0	20.0
Total		20.8	22.0	51.6	10.0	27.8	41.0	10.0	12.8	195.0	17.0	48.6
Liver	Total Body	11.0	5.0	8.0	8.0	7.0	8.0	16.0	19.0	5.0	21.0	3.0
Spleen	" "	2.0	2.0	1.0	2.0	2.0	3.0	2.0	2.0	5.0	2.0	1.0
Marrow	" "	0.7	0.9	2.0	0.2	1.0	2.0	0.1	0.1	15.0	0.3	2.0
Blood	" "	6.0	7.0	19.0	2.0	10.0	14.0	0.5	1.0	5.0	2.0	19.0
Total		19.7	14.9	30.0	12.2	20.0	27.0	18.6	22.1	30.0	25.3	25.0
Liver	Gonads	4.5	2.2	3.4	0.8	0.7	0.8	1.7	7.9	2.2	2.3	0.3
Spleen	"	0.4	0.6	0.3	0.1	0.1	0.2	0.1	0.4	1.5	0.1	0.1
Marrow	"	1.1	1.3	3.4	0.0	0.2	0.3	0.0	0.2	22.6	0.1	0.4
Blood	"	6.5	7.8	20.7	2.7	10.7	16.1	0.5	1.3	5.2	2.7	21.5
Total		12.5	11.9	27.8	3.1	11.7	17.4	2.3	9.8	31.5	5.2	22.1
Blood*	Blood	16.4	19.7	52.6	5.2	26.3	39.4	1.3	3.3	13.1	6.6	52.6

*non-penetrating dose only

Table 3

Patient	Diagnosis
A	Pure red cell aplasia
B	Red cell aplasia (in remission)
C	Red cell aplasia (in remission)
D	Suspected red cell aplasia
E	Suspected red cell aplasia
F	Suspected red cell aplasia
G	Suspected red cell aplasia
H	Refractory anemia
I	Refractory anemia-marrow storage disease
J	Refractory anemia-liver storage disease
K	Normal

Summary (mrad/μCi)

	Liver	Spleen	Red Marrow	Gonads	Blood	Total Body
Vanderbilt	77-426	173-395	10-195	2-32	1-53	12-30
Berlin (1973)	100	130	-	27	22	22

c. Dosimetry of I-131 Hippuran in Bi-lateral and Transplant Renograms

The I-131 labelled hippuran renogram has been a routinely-used clinical test to assess renal function for a number of years. We have been investigating the calculation of the radiation dose associated with these studies for patients with two kidneys (bi-lateral) and transplant patients. The transplant patient presents a particularly interesting problem in that renal function may vary dramatically from essentially no function to normal function within a matter of a few weeks. At Vanderbilt Medical Center there is a very active transplant program with an average of 4-6 in-patients under constant study and observation at any time. As a part of the post operative procedures, the transplant patients have I-131 hippuran renograms performed every other day until the acute rejection period is passed and then less frequently for an extended period on an outpatients basis.

In order to carry out these studies we have employed a mathematical model to fit the data from the patient studies and to simulate the hippuran kinetics in situations where the renal function varied from no function to completely normal function. Using these calculations we are continuing to make dose extimates on specific patients and are making dose estimates as a function of renal function from the model simulations.

The model we have chosen was adapted from the model suggested by Lindmo, et. al. and is shown schematically below:

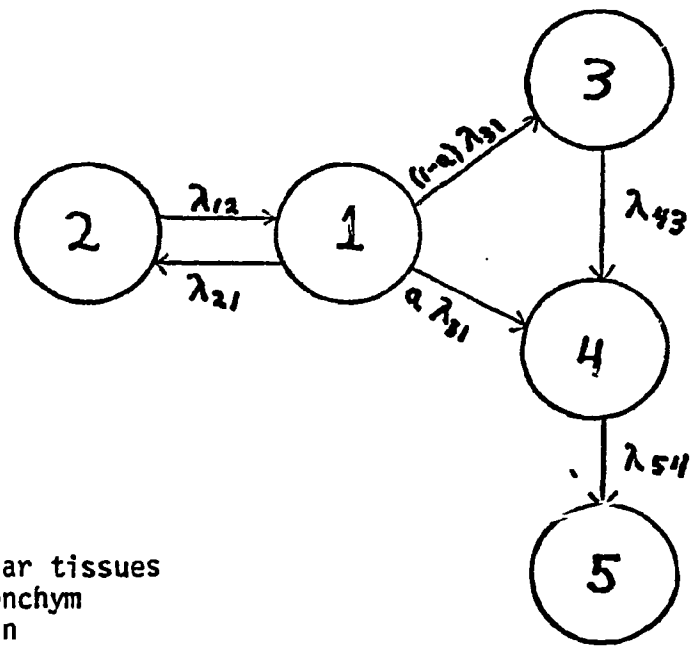

1: Plasma
2: Extra vascular tissues
3: Tubular parenchym
4: Tubular lumen
5: Bladder

Patient data were collected by means of an Anger Camera placed anteriorly over the kidneys and bladder. In addition a stationary probe is placed over the heart to monitor the blood pool activity. A second probe if needed is placed over the bladder catheter when one is present in order that the total bladder activity may be measured.

Using the flow parameters shown in Table 1 for normal renal function, the values of the renal uptake ($\lambda 31 + \lambda 41$) and excretion ($\lambda 54$) rates are slowly varied and the resulting renograms were generated.

Two such simulated renograms are shown in Figure 1. The upper curve is for the extreme case where the kidney retained a normal extraction or uptake while the excretion capability was completely lost. The lower curve displays a normal function. The radiation dose derived from these two simulations is shown in Table 2. Although the maximum dose of 45 rads is possible, none of the transplant patients we have measured have estimates greater than 8 rads.

In the clinical environment the transplant patient is studied every other day until normal or a clinically adequate function is reached. A set of typical transplant renograms covering a two weeks period is shown in Figure 2. For each patient flow parameters are computed and the radiation dose is calculated from the 30 minute renogram data plus the measured residual activity prior to each succesive study. Figure 3 shows the comparison of the computer model calculations to the observed data shown in Figure 2 at Day 10. As part of the model calculations, the computer utilized data for the blood pool clearance of the I-131 hippuran as monitored by a probe positioned over the heart. These data are shown in Figure 4.

Data from each patient was summarized as a function of time post transplantation and the average radiation dose to the kidney was calculated. A typical plot of kidney dose versus time after transplantation is shown in Figure 5. The upper curve corresponds to a case where the kidney responded very slowly and consequently resulted in continued large kidney doses finally converging to the normal radiation dose of approximately 60-80 mrads. The lower curve was obtained from a patient who responded rather quickly and approached normal function within 12-14 days. Difficulty arose in estimating the excretion parameter which corresponded to washout half-time's from 2-8 hours. For these studies the 30 minute renogram was inadequate to determine a non-zero washout rate while the rates were in fact fast enough to bring the residual to $\leq 1\%$ of the injected dose when measured at the 48 hour renogram. For these cases we have estimated the mean dose to be: 1.0 ± 0.6 rads

The range of radiation doses to the kidney during the first 1-3 days usually ranged from 1-8 rads. After this time, dose estimates ranged from 0.1 or about normal to the maximum for those kidneys which failed to function. Dose estimates to the gonads and bladder are also being calculated. These studies will be extended to an extensive study of patients viewing bi-lateral renograms in order to relate the absorbed dose to function impairing kidney disease as well as to renal obstruction.

Table 1

TRANSPLANT KIDNEY MODEL PARAMETERS

FOR NORMAL FUNCTION

λ_{12}	0.095/min
λ_{21}	0.072
λ_{31}	0.092
λ_{43}	0.388
λ_{54}	0.500

Table 2

I-131 HIPPURAN RENOGRAM

(50μCi Dose)

	Dose in rads to the kidney
Normal Function	0.078
No Excretion	44.9

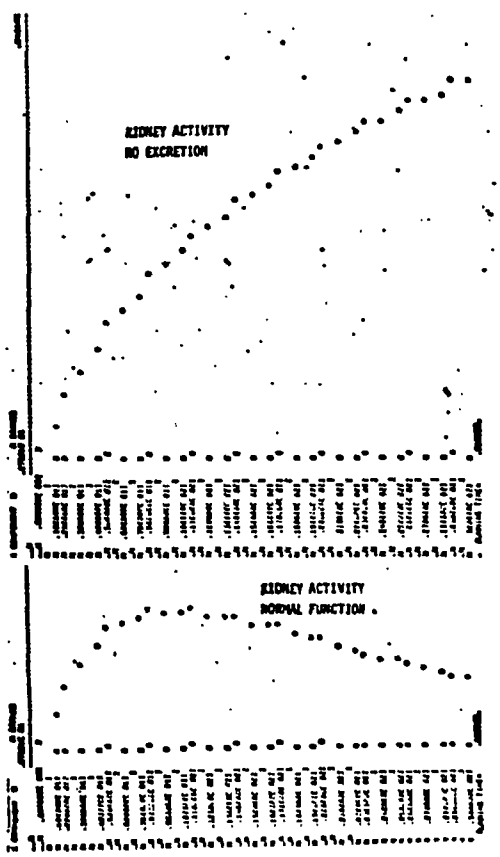

Figure 1.

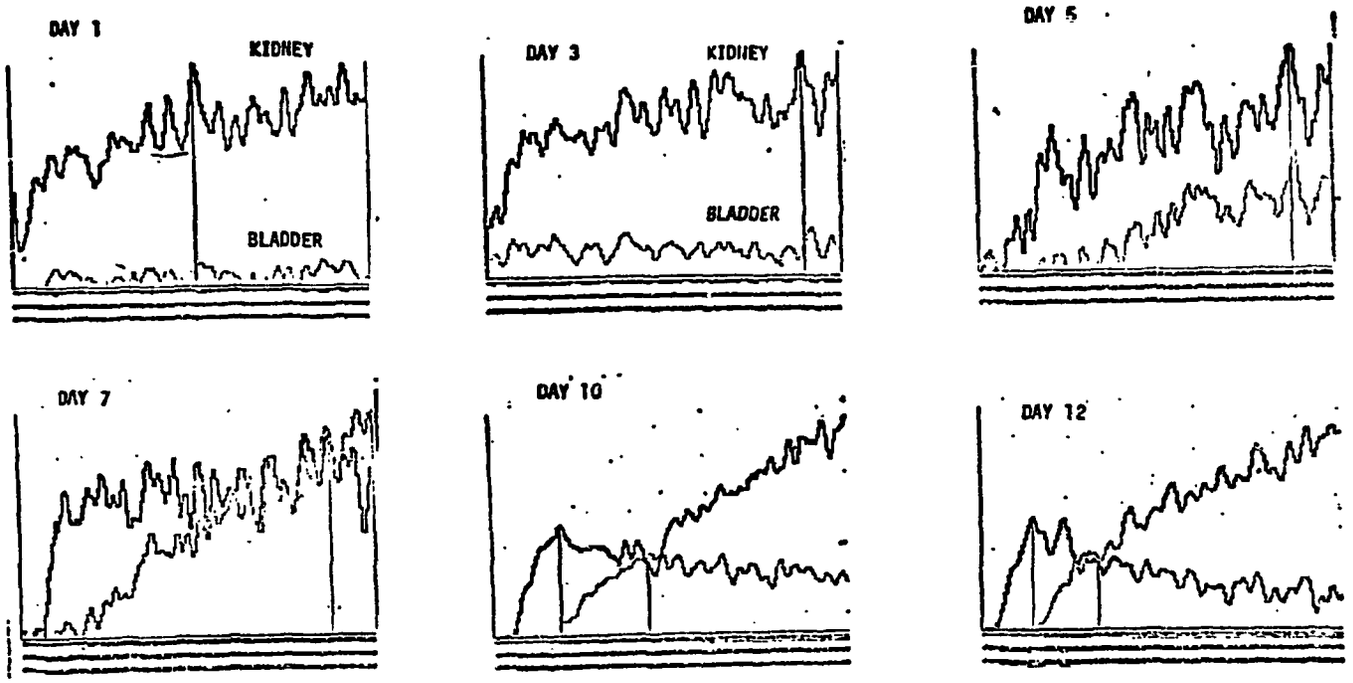

Figure 2. Transplant Renograms

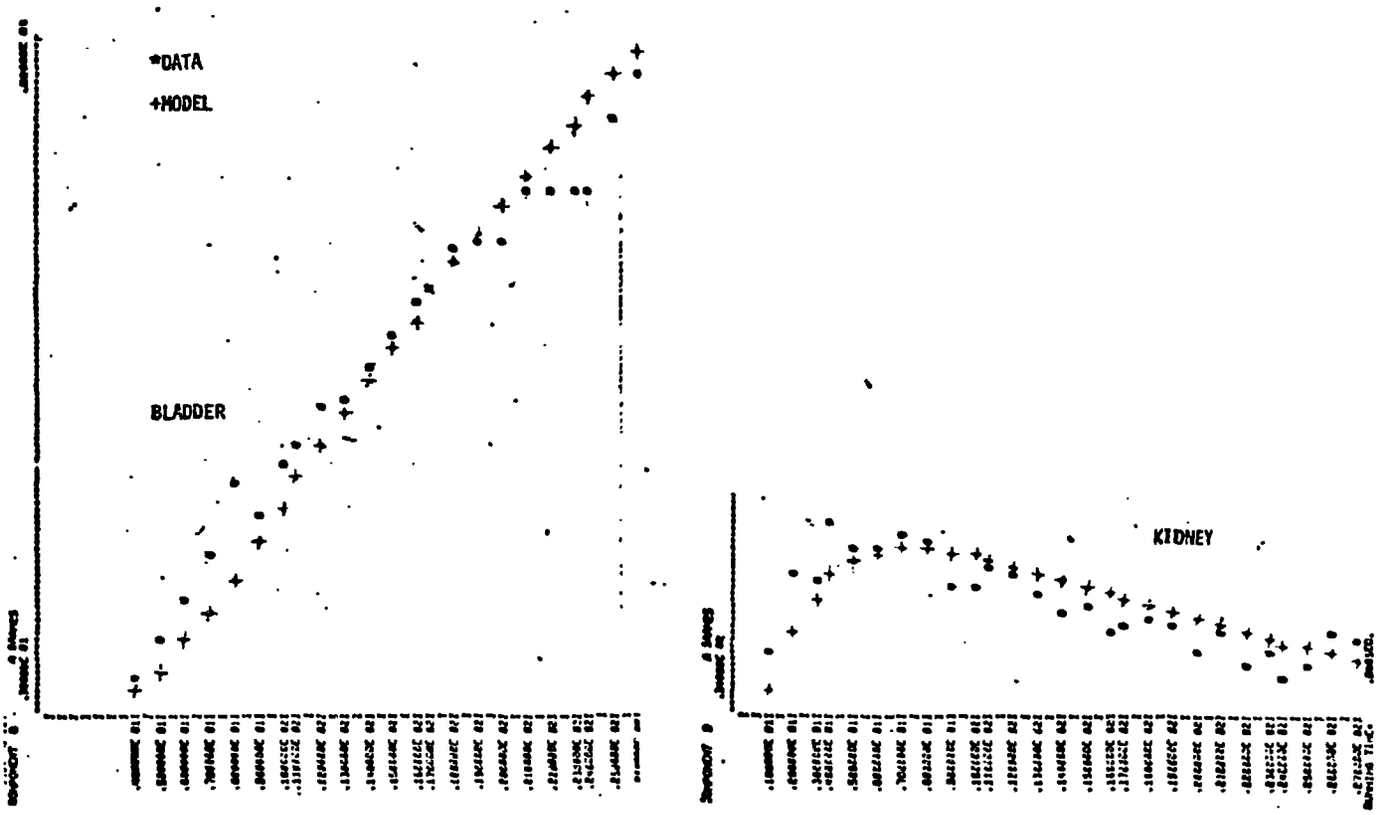

Figure 3.

STATIONARY PROBE DATA
CORRESPONDING TO PREVIOUS FIGURE

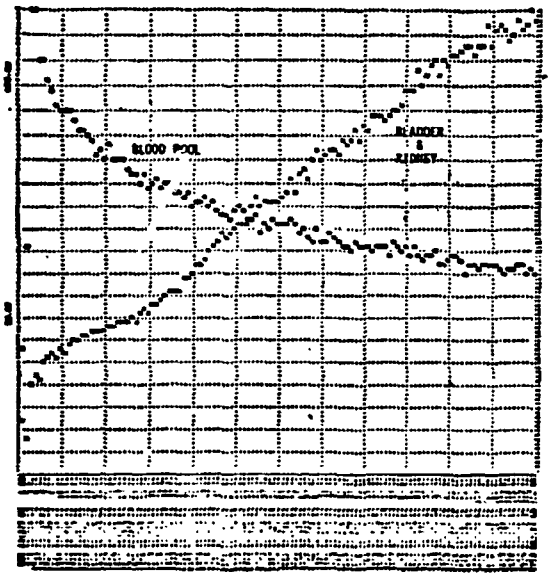

Figure 4.

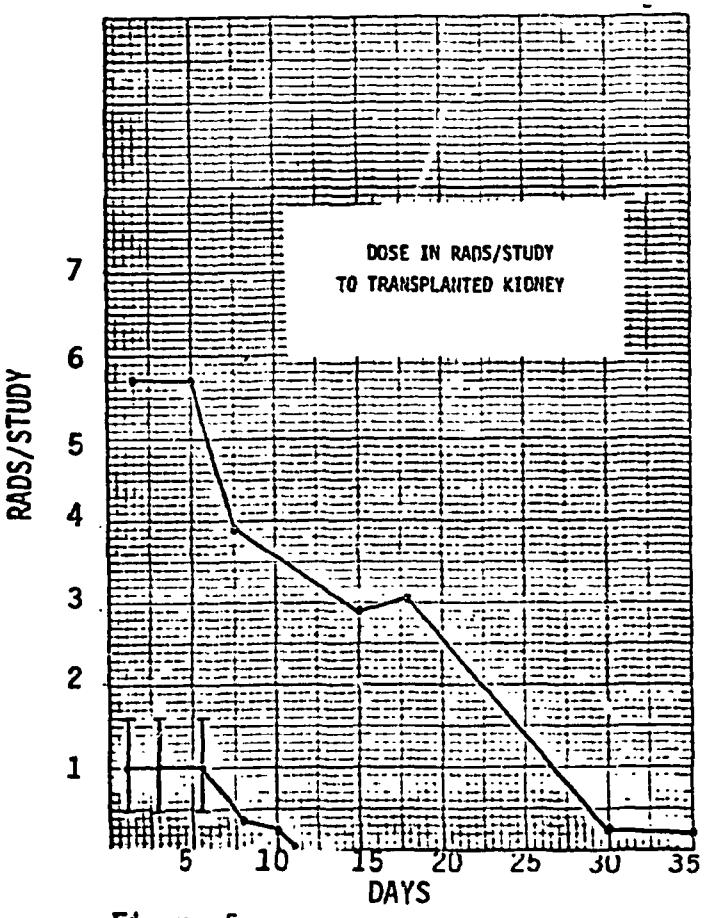

Figure 5.

d. Dosimetry of Tc-99m Labelled Pyrophosphates

Much interest has been shown recently in Tc-99m Pyrophosphate as both a new bone scanning agent and as an agent for assessing myocardial infarctions. Initial data indicate that the blood to bone ratio may be improved for Tc-pyrophosphate relative to the more routinely used agent Tc-polyphosphate. Initial data on short term blood clearance and urinary excretion exist; however, long term biological retention data are not available. We propose to study 8-10 volunteers during the next year according to the protocol shown in Table 1. These volunteers will be selected from patients referred to the Division of Nuclear Medicine for routine bone scans. After informed consent has been obtained the patient will be followed for 48 hours post injection using the whole body counter, whole body scanner, blood samples, and scintillation camera images. Preliminarily results from a pilot study are shown in Figures 1 and 2. These data reveal a multi component blood disappearance curve and a total body curve consisting of at least two components. The shortest of the two components for the total body has a $T_{\frac{1}{2}}$ of 3-6 hours while the longer is $\geq$ 72 hours.

Although both of the two preliminary studies showed similar behavior as to the number of exponential components or compartments and the sizes of the washout rate constants, the initial distribution of the pyrophosphate appears to be different. The fraction in the rapid compartment was 0.75 in one study while it was found to be 0.55 in the other. Similarly the slow compartments showed 0.25 and 0.45, respectively. Preliminary dose estimates assuming the radioactivity to be uniformly distributed in the total body dose of 75-90 mrem/mCi administered or 0.75-0.90 rem per study with an administered dose of 10mCi.

These studies are just beginning and as more data becomes available the radiation dose to the gonads, skeleton, bladder, red marrow in addition to the total body will be determined.

TABLE 1

PYROPHOSPHATE PROTOCOL

Step 1. Determine plasma volume with I-125.

Step 2. Inject ^{99m}Tc-pyrophosphate (15 mCi) and collect data as per protocol below.

TIME	BLOOD SAMPLE	W.B. SCAN	W.B. COUNT	PIN-HOLE CAMERA THYROID & ANKLE
15-20 minutes			X	X
2 hours	X	X		
6-8 hours	X		X	X
24 hours	X		X	X
48 hours	X		X	X

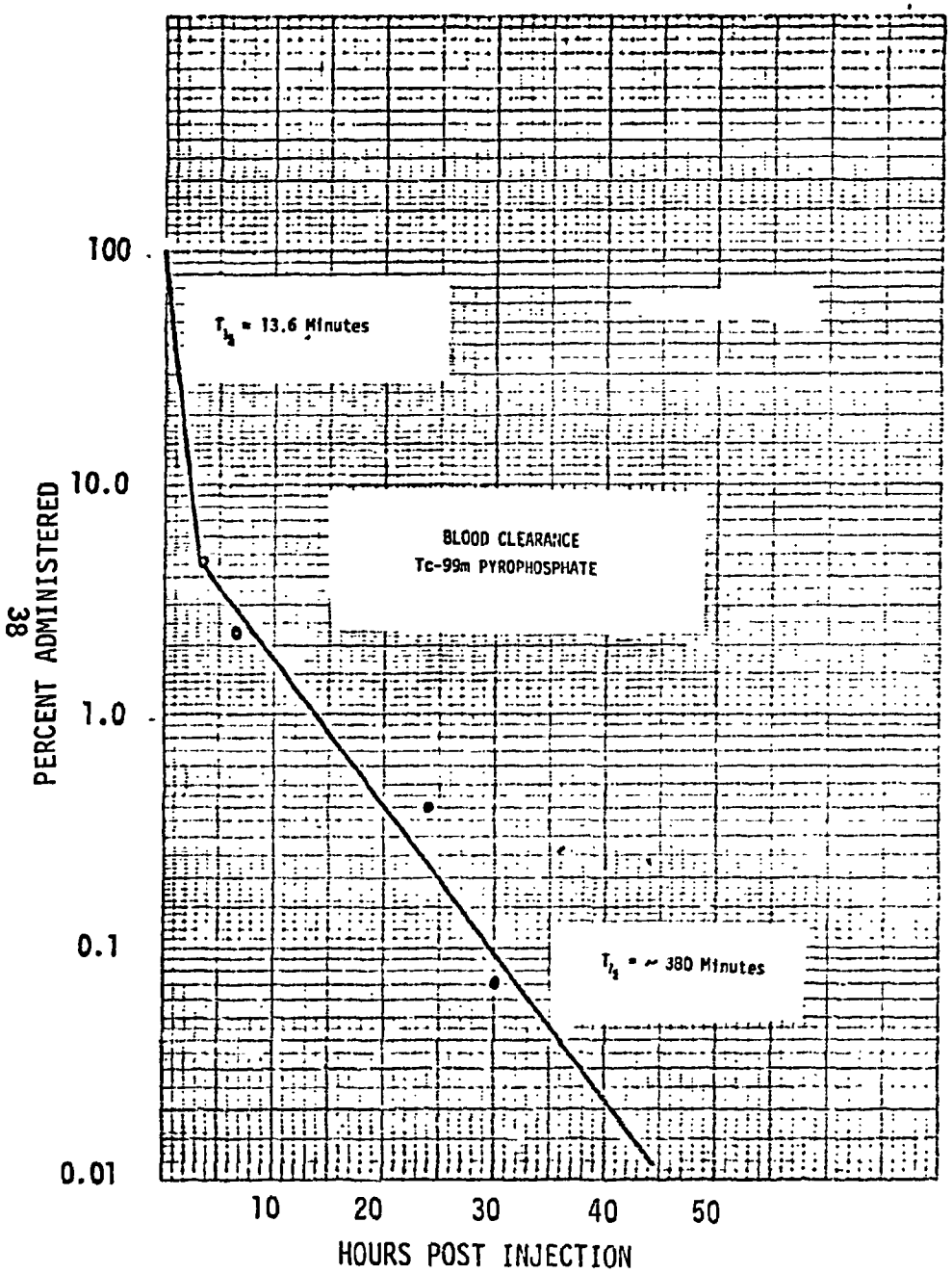

Figure 1

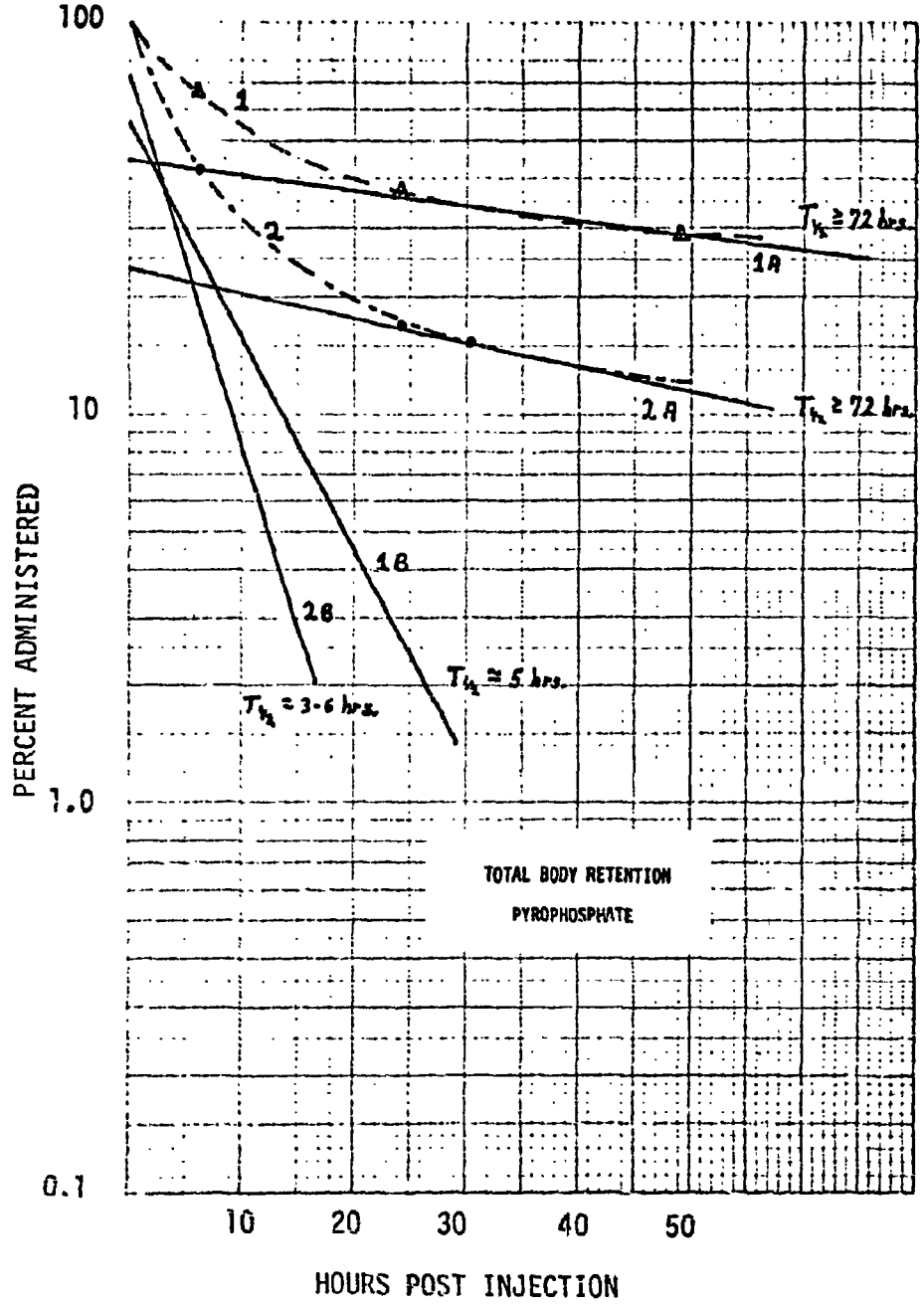

Figure 2

e. Neutron Dosimetry from Fluorescent Thyroid Scanning

Fluorescent scanning of the thyroid has been performed routinely in our department for several years. In this technique the thyroid gland is irradiated point-by-point by an external source of radiation (Am-241) and the characteristic x-rays of iodine produced in the thyroid are counted by a high resolution lithium-drifted silicon detector. The resulting image obtained is an intensity map corresponding to the stable iodine distribution of the thyorid. One of the primary advantages of this system is the low radiation dose to the patient (50 millirads to the thyroid and limited to the neck region). However, it has been pointed out by Robinson, et. al.[1] that there may also be a neutron dose associated with the scanning procedure. This is due to the fact that the Am-241 used in such studies is usually encapsulated as a pellet of americium dioxide compressed with powdered aluminum as a binder. Thus the aluminum presents a target for the α-particles emitted from Am-241 for the reaction $^{27}Al(\alpha,n)^{30}P$. Our fluorescent source consists of 15 disk sources each 0.75 inches in diameter doubly encapsulated in stainless steel. Each source contains 1 Ci of Am-241. We were concerned about the possibility of a neutron exposure hazard from this system and sought to detect the presence of a nuetron flux and to measure the magnitude of the resultant exposure.

A BF_3 proportional counter (Deuter Stokes Model RSN-44A) was used for the detection of the neutrons as a Rem counter was not available. This counter has a thermal neutron sensitivity of 28 counts/sec per unit thermal flux. The produced neutrons will possess a spectrum of energies up to about 10 MeV. For fast neutrons, due to the increasing KERMA with energy and decreasing quality factor, to a good approximation, a fluence of 3×10^4 n/cm^2 is equivalent to a dose of 1 millirem. Therefore a fast flux of approximately 8n/cm^2/sec is equivalent to 1 millirem/hour.

We observed a miximum count rate with with our BF_3 detector 20 cps at ~17 cm from the Am-241 source (The eyes are normally about 20-23 cm from the source). Approximately 5 cm of wax was used to moderate the neutrons. As the detector was rather large (12" active length, 2 inch diameter) there are some problems with geometry. However, assuming only 3% of the nuetrons are thermalized, the patient dose to the eyes for a 20 minute scan is less than 1 mrem.

This number is consistent with the results of Robinson for our different source configuration and strength, and is well within the safe region of exposures.

[1] Robinson, E.L., Hannal, B.O., Bass, W.B., and Wills, E.L. Health Physics 26 (April) pp 301-306.

f. Integration of Ultrasound with Scintillation Images

We have previously reported an error due to self-attenuation of a depth-distributed source which occurs when one tries to regard the source as being equivalent to (i.e., gives the same detector count rate as) a point source of the same activity at an "effective" depth within a scattering medium. For an assumed distribution of activity, such as a uniform distribution, the correction for this error requires a knowledge of the source thickness. This can be found from emission scan data if the radionuclide being counted emits at least two strong, well-resolved photopeaks that are counted separately; however, Tc-99m emits only one. Therefore, ultrasonic scans were used to determine the source thickness for this particular study (Tc-99m sulfur colloid in liver).

The scanner itself (Unirad Corporation) contains both the wave source and detector in the same probe. The ultrasound is emitted as pulses which enter the body, and those reflected back to the probe are analyzed (by the scanner electronics) by measuring the elapsed time of the round trip for a particular pulse. From this time, the scanner determines the distance from the probe to the reflection point, and also records the direction in which the probe is pointing. By moving the probe in a plane across a patient, one generates a cross-sectional picture of the reflecting structures, which is displayed on a storage tube and photographed for later analysis.

The probe is mechanically constrained to free movement in a plane only, although one can pick whatever plane is desired. For this study, a set of planes transverse to the body and intersecting the liver were used. Thus each picture gave a cross-sectional view of a portion of the liver (see figure 1), and from the calibrated scale on the storage tube, an estimate of the liver thickness as a function of position was easily found.

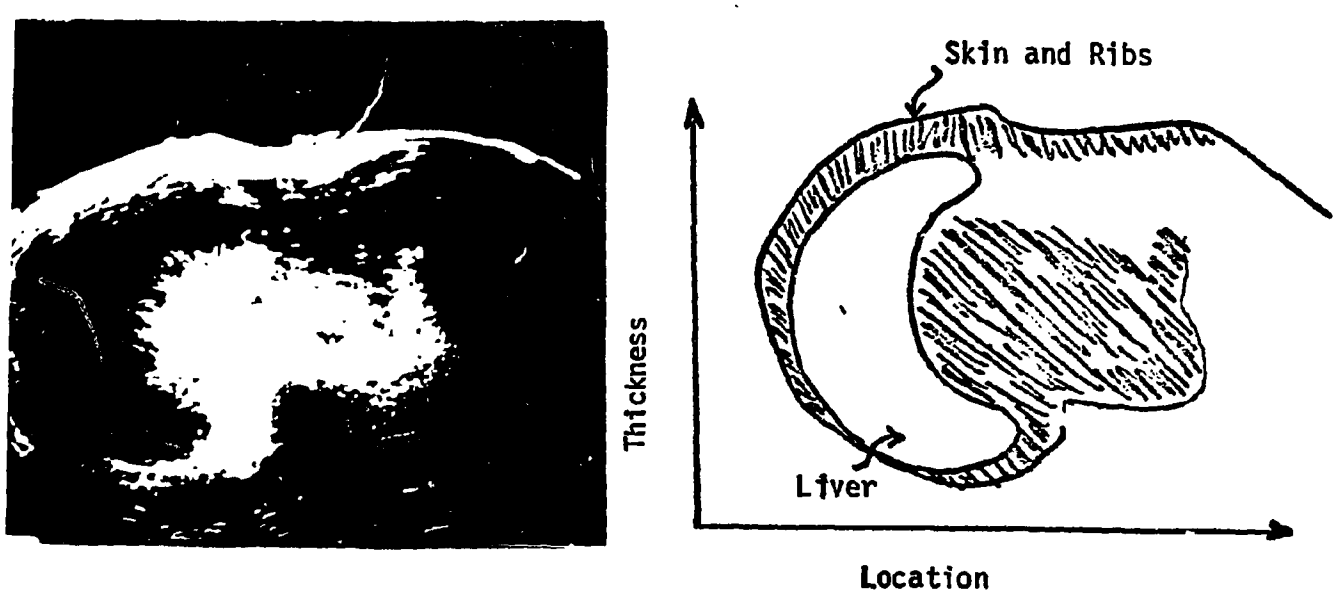

Figure 1. An ultrasonic scan of the liver is on the left, and an interpretive sketch is shown on the right. A distance of one centimeter on the picture corresponds to four centimeters in the patient.

Since the distance from the probe to a reflection point is determined from a time measurement, the distance determination depends upon the speed of ultrasound in the reflecting medium. This, in turn, will vary from one medium to another. Our scanner is calibrated on the assumption that the ultrasound traveled through water, and so would give erroneous results for media having a different propagation speed. To illustrate this, solid lucite cubes of different thicknesses were scanned, and gave the results shown in Table 1.

Table 1.

True Thickness (cm.)	Measured Thickness (cm.)	True/Measured
2.54	1.4	1.8
2.9	1.7	1.7
3.2	1.8	1.8
3.9	2.2	1.8
5.0	3.0	1.7

Average = 1.76 or 1.8 cm.

Here, the first column is the actual cube thickness, the second is that measured from a scan picture, and the third is the ratio of the first two, to two significant digits. Since the speed of ultrasound in lucite is about 2680 m/sec., and only about 1480 m/sec. in water, for a ratio of 1.81, the error above is mostly due to this speed difference. So, to obtain accurate liver thicknesses, one must multiply the scan-deduced thickness by the ratio of the speed of ultrasound in liver (1549 m/sec.) to that in water, a correction of only 4.8%.

The generation of ultrasonic pictures of suitable quality caused some problem because of the complex reflection geometry of the body and the attenuation of pulses as they traveled through the body. Reflections from the front of the liver tend to be obscured by the many strong reflections from skin and ribs. Reflections from the back of the liver have to cross several acoustic interfaces (including ribs and skin), which makes them both weak and few in number. The amplitude of the emitted pulses can be varied to give fairly strong pulses from deep in the body, but this also increases the interference from rib reflections and multiply-reflected pulses, and does nothing to increase the number of pulses from reflections deep in the body. However, the scanner also has the ability to discriminate against pulses on the basis of arrival time, so that interference from surface structures (ribs) can be minimized. This discrimination is done only on the basis of arrival times shorter than a set time, so multiply-reflected pulses can still be a problem. Thus, one must manage between the extremes of obtaining few pulses from reflections deep in the body, and a "washed out" picture from internal reflection in the organ being imaged. The former shows little in the way of liver shape, as does the latter.

Trial and error was used to obtain pictures of suitable quality. This was facilitated by the ease of generating a picture ($\leq$ 30 sec.) and lack of patient discomfort. As more experience was gained by the operator, less time was required to produce acceptable pictures.

To illustrate the effect of multiple reflections, a scan of a water phantom was made, taking care to keep the probe normal to the bottom of the phantom. The resulting image is shown in Figure 2, along with an interpretive drawing.

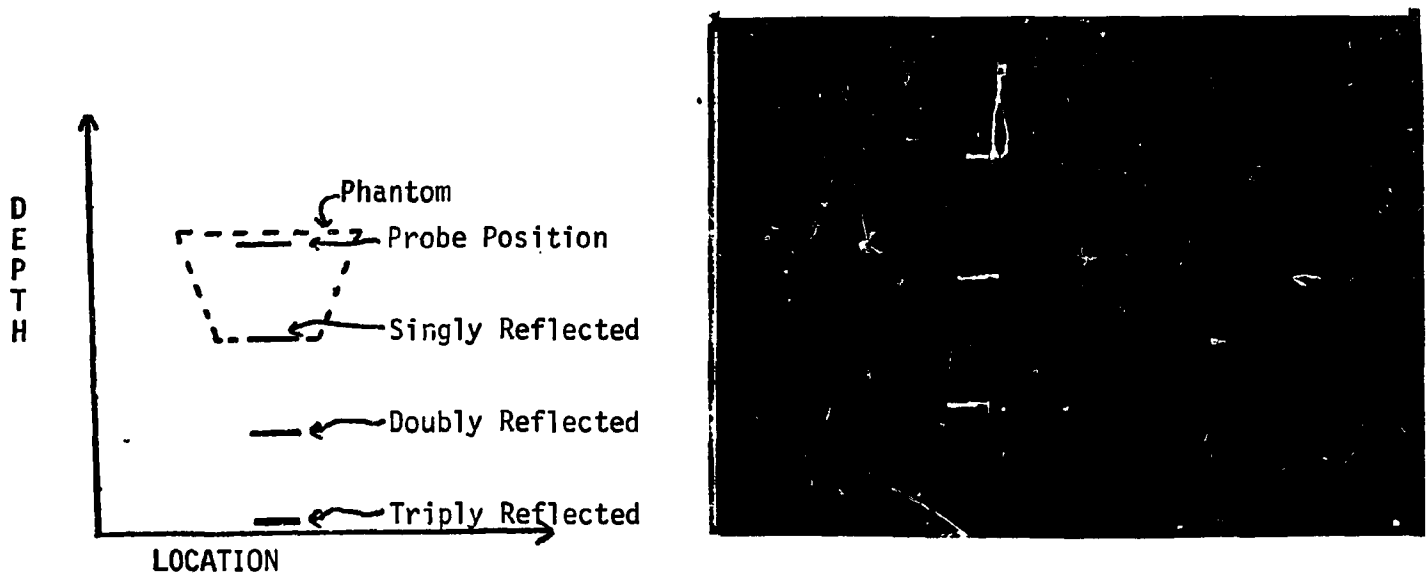

Figure 2. A "good geometry" ultrasonic scan of a water phantom, showing the presence of multiply-reflected pulses.

As can be seen, multiply-reflected pulses were detected, which due to their longer arrival times, are displayed farther from the probe. The singly reflected pulses are those which made only one round trip from the probe to the bottom of the phantom and back before being detected. The doubly reflected pulses made two roundtrips before detection, and are recorded as being from a structure twice as far away. Similarly, the triply reflected pulses are recorded three times as far away. The multiply-reflected pulses could be minimized by changing the scanner settings, as shown in Figure 3a. In Figure 3b, the same scanner settings were used as in 3a, but the probe was rotated to create reflections from the sides of the phantom.

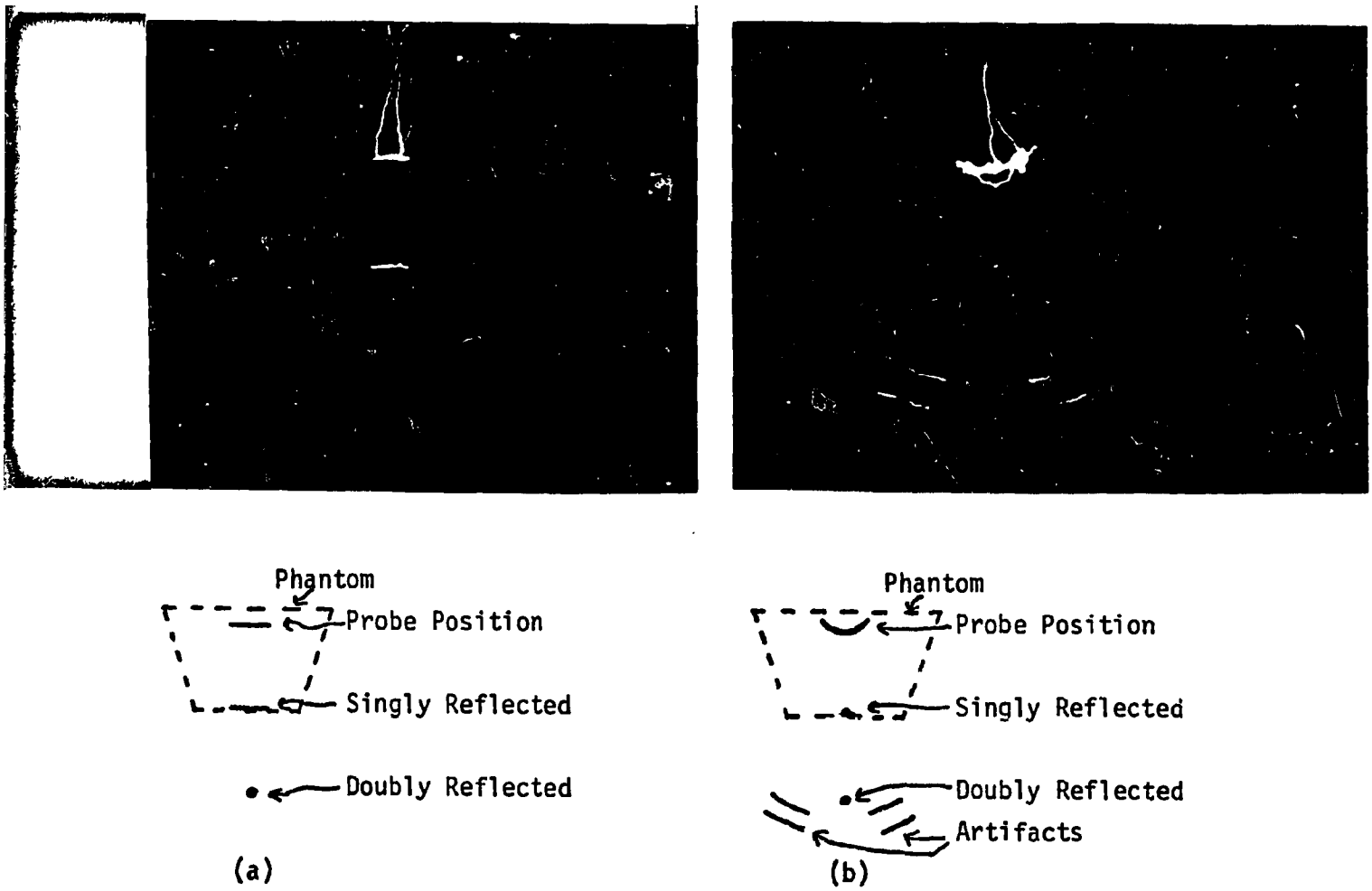

Figure 3. Water phantom scans, showing minimization of multiply reflected pulses (normal incidence) in (a), and the presence of artifacts with non-normal incidence in (b). Both scans were made with the same phantom and instrument settings.

Here, singly reflected pulses were recorded only when the probe was normal to the bottom of the phantom, as one might expect, but several artifacts were produced for other orientations. Since the artifacts are located beyond the phantom, they must be due to complex multiple reflections. For liver imaging, the ultrasound must pass through different media of irregular shape (skin, muscle, ribs, liver tissue), so artifacts due to multiple reflections from ribs and the anterior liver wall might obscure the image of the liver boundaries. In judging a picture for acceptability, then, one should be suspicious of equally spaced or concentric image features, as well as requiring suitable contrast. Just how much these factors affect the magnitude of the self-attenuation correction is unknown, but the correction itself is expected to be in the range of 10% to 20%. This corresponds to an average liver thickness of 5" to 8", so that ultrasonic data should give a reasonable correction.

g. Solid State Dosimetry

The dosimeters used in the Tc-99m sulfur colloid studies are LiF TLD's (TLD-100, 1/8" x 1/8" x 0.035"). Since these are not absolute-reading dosimeters, it is necessary to calibrate their light output per unit dose by empirical means. The geometry chosen for this calibration was a uniform cube source of Tc-99m, with the dose being computed to a 2" x 2" x 0.035" thick slab of LiF placed concentric to a face of the cube (2" square slab on 3" square face). The dose computation was made with the same Monte Carlo technique that was used to calculate patient doses, thus allowing a more direct calibration than would be obtained with ionization chamber readings. To check the accuracy of these cube calculations, we compared the TLD output/dose for the cube problem to that from a "point" Tc-99m source and ionization chamber readings. As reported last time, these two results were a factor of three apart.

We consulted with Dr. J. W. Poston of the Health Physics Division of ORNL about this discrepancy, and he led investigation of the accuracy of the computer calculations at ORNL while we investigated the accuracy of the TLD readings. As a result, the causes of the discrepancy were discovered and satisfactory agreement between the cube results and "point" source results obtained. The difficulties were caused by a subtle, but large, error in the computer calculations, and a smaller, but still significant error in the TLD readings.

Basically, the computer calculations were in error due to a modification designed to reduce the time necessary to get good statistics for the thin LiF target region. Monte Carlo methods were used to find the flux across the target region, from which the dose was calculated by analytical means. After much discussion, it was decided to do a calculation in exactly the same manner described in MIRD Pamphlet #5, i.e., calculate the dose from interactions which occur within the LiF volume. This would serve as a check on the dose calculated from energy flux, and gave the results shown in Table 1.

Table 1

Dose from energy flux calculations	1.059×10^{-13} Rads/photon
Dose by MIRD #5 method	2.132×10^{-13} Rads/photon
Dose inferred from earlier "point" source TLD readings	$\sim 2.8 \times 10^{-13}$ Rads/photon

Clearly, the energy flux calculation was greatly in error, with the direct (MIRD #5) method giving results more in accord with the TLD readings. The reason for this error is not clear, but in all later calculations, the direct method was used.

At the same time, we discovered an error in the TLD readings which accounted for the remaining discrepancy. Our investigation began with the observation that whenever a large group of TLD's (> ~50) was read out, the last few would read appreciably lower than the first few by 10-20%. This was true

regardless of the order in which they were read, so this decrease was not due to the TLD's themselves. Then a group of ten TLD's was annealed, exposed to 137-Cs γ-rays, and read out, with this cycle repeated twice more. The results are shown in Table 2.

Table 2

	True Exposure	Exposure from Average of TLD Readings
First Readout	580.8 mR	580.8 mR (calibration exposure)
Second Readout	33 mR	31 mR
Third Readout	33 mR	29 mR

Just as interesting as the steady drop of the TLD-inferred exposures was the fact that the standard deviation of the TLD readings was $\sqrt{3}$ mR for both the second and third readouts, suggesting that the problem was not due to the low light levels resulting from 33mR exposures. The suspected cause was the silver heating pan of the reader, since visual inspection showed it to be dirty. This was first checked by thoroughly cleaning the pan, and then inspecting it during personnel badge readout by the Radiation Safety Office. After the first TLD was read, a faint imprint of exactly the same size and shape of a TLD could be seen on the pan. The next few TLD's were placed over this imprint, which became steadily whiter. By the time all the personnel badges were read ($\sim$ 200), almost all of the pan was covered with this white material. Evidently, each TLD was chemically reacting with the silver pan, producing a substance (probably AgF) which reflected less light than the shiny silver. Since some of the detected light would be reflected off the pan, this increasing dirtiness would tend to lower TLD readings as more of them were read.

The results in Table 2 indicate that this change is rather small, and approximately linear, for a group of ten TLD's per readout. So it was decided to correct for this effect in the following way:

1. Read out two "standard" TLD's (given a known dose) in a clean pan. Then all other readings would be corrected to this "standard" pan.
2. Before reading out a group of TLD's, clean the pan if necessary.
3. Read out the first "standard" TLD.
4. Read out the group of TLD's.
5. Then read out the other "standard" TLD.

The reading obtained by #3 would give the pan reflectivity, as compared to the "standard" pan, before the group was read, while #5 would give similar information after the group was read. Then assuming that the pan reflectivity changed at a constant rate, a correction for each TLD in the group could be made, provided that the "standard" pan did not get appreciably dirty for the second "standard" TLD reading.

This correction method was checked using a group of calibrated TLD's exposed to 33 mR. The correction implied by #3 above was 4%, and the pan reflectivity was calculated to be decreasing at the rate of .15% per TLD read. The corrected TLD-inferred exposure was 33.3 mR (1% error), with a

standard deviation of 1.7 mR ($\sim \sqrt{3}$ mR again). Had the correction not been made, the TLD-inferred exposure would have been 4% in error, because of the pan cleaning. So it appeared that cleaning the pan and making a correction based upon #3 is the most important factor, especially if correlations between TLD readings made several days or weeks apart are to be made.

The cube problem was then run using this correction. The dose implied by the TLD readings was 2.325×10^{-13} rads/photon, only 9% different from the computer values found by Dr. Poston, and when the uncertainties were considered, these results were within a standard deviation of one another. This is felt to be satisfactory agreement.

Next it was decided to make a more detailed investigation of the reproducibility of TLD readings, because a knowledge of the reproducibility would be very important in the Tc-99m sulfur colloid study. In addition, a more direct check of the assumed linear rate of reflectivity change would be desirable.

Difficulties appeared immediately, with unusually large pan corrections being made ($\sim$ 10% to 30%), although the corrected TLD readings were usually reproducible to within ±2%. However, an unexplainable 10% error was seen on occasion. The effects of the exact position of a TLD in the pan were investigated (it made little difference) as well as the cleanliness and optical clarity of each TLD (which appeared to account for most of the $\pm$ 2%). In further studies, the pan appeared to sometimes get more reflective as more TLD's were read, rather than less, making the assumed linear rate of reflectivity change suspicious.

To check this, three "standard" TLD's were used. The five steps shown above were followed, with the third "standard" TLD read after step 5. From this, two values of the rate of reflectivity change could be found and compared. These never were the same, and often one was positive while the other was negative (although both absolute values were 4% or less of the correction found from step 3). This was surprising, in view of the cube problem and the 33 mR exposure results.

With three "standard" TLD's, and the assumption of a linear dependence, it is not necessary to assume that the rate of reflectivity change is small- there is enough information to compute the rate the "standard" pan changed and the rate the pan changed when reading out a group of TLD's, as shown in Appendix I. So a group of five TLD's was read out, with the first, fourth, and fifth being "standard" TLD's. The readings implied that the "standard" pan had gotten less reflective at a rate of 26.9% per TLD read. Consequently, the linear assumption is wrong (the correction goes negative after four readings), but note that the rates for these two readouts are nearly the same. Apparently, this was the usual case, giving the ±2% reproducibility seen earlier. But if this did not always happen, it could explain the 10% errors sometimes seen. This point was not checked, since a different correction method was going to be devised anyway.

Before discussing the new method, first consider the chain of relationships involved which comprise the relationship between a TLD readout and the TLD dose. One has the TLD dose → light emitted by the TLD → light detected

by the PM tube → total charge delivered by the PM tube (the number obtained from the readout process). In order to have good reproducibility, one clearly must be able to correct for changes that may occur along this chain. The first part depends upon the inherent properties of each TLD as a phosphor, as well as its optical clarity, cleanliness, and the type of heating cycle used. The next part depends upon the pan reflectivity and the geometry of the pan, TLD, and PM tube setup, while the last part depends upon the PM tube gain and the performance of the other electronics of the reader. With our reader (model TLR-5, Eberline Instrument Company), an internal light source is used to easily check and correct for variations in this last part, so the correction method is primarily intended to check the other parts of the chain.

To so this, one simply reads out a "standard" TLD between each TLD of the desired set. For the calibration readout, one first reads the first "standard" TLD, then the first TLD being calibrated, then the second "standard" TLD, then the second one being calibrated, and so on until all the TLD's of the set have been read, followed by the last "standard" TLD. To determine a dose with these calibrated TLD's, the same readout process is used, with the same TLD's being read in exactly the same order as before. Comparison of corresponding "standard" readings would give correction factors for differences in the chain of relationships, and the interpolation of these correction factors would give estimates for correcting the reading of each calibrated TLD.

In order for this method to be effective, changes in the chain must occur in a smooth, continuous fashion. However, the buildup of dirt on the TLD's and brief fluctuations in line voltage might not meet this condition, so special care was taken to keep the TLD's as clean as practical, and if opaque spots were noted on a TLD, it was always placed with the same side down against the pan. The line voltage was also monitored, and observed to fluctuate unpredictably between 110 v. and 120 v., which was enough to affect the heating components of the reader and its cooling fan. Since this might also affect the charge-collection and counting electronics, a variable power transformer was used to keep the reader voltage between 119 v. and 120 v. This seemed to be significant, because before the transformer was used, the reader would sometimes cut off prematurely (about once every 100 readings). Since the transformer has been used, no premature cutoffs have occurred (about 300 readings to date).

To test this method, as well as to check for the effects of the TLD's becoming dirty, a group of five TLD's was exposed and read repeatedly (and pre-annealed for 1 hour at 400° C each time). The pan was cleaned for the calibration readouts, and the results of the succeeding readouts are shown in Table 3. The first, third, and fifth TLD's were used as the "standard" TLD's, while the second and fourth were the ones tested for reproducibility. The table entries are the percent error of the TLD-determined dose from the actual dose.

Table 3. Percent Errors from Calibration Exposure

	Corrected Readings			Uncorrected Readings		
Trial #	TLD #2	TLD #4	Dose (mrad)	TLD #2	TLD #4	Cleaned Pan?
1	+ .46	+ .28	430	-3.5	-3.7	No
2	+ .58	- .91	488	-1.4	-3.0	No
3	+ .39	+2.8	32	+2.4	+4.8	No
4	-1.2	+5.5	523	+ .8	+7.5	No
5	- .33	+2.7	412	+4.7	+7.7	Yes
6	-2.2	+ .08	463	+2.8	+5.1	No
7	-2.3	+1.5	522	+ .7	+4.5	Yes
8	- .69	+ .28	355	+2.3	+3.3	No
9	.00	+1.1	507	+5.0	+6.1	Yes
10	- .74	+4.0	35	+2.3	+7.0	No
Average	.89	1.9		2.6	5.3	

On the whole, the corrected readings were less in error, and the largest errors in the corrected readings tended to occur when the pan was not cleaned. Trials 1-4 show that the error gets worse as the pan gets dirtier, particularly for TLD #4. Further, note was made of the dirtiness of each TLD each time. TLD #2 was relatively clear, while TLD #4 was not. The dirt spot(s) on TLD #4 varied in size and color (black ↔ white) from trial to trial, probably because of the effects of the 400° C anneal. This is probably why it had a larger average error, whether corrected or not. The size of the dose does not appear to make much difference, although more trials in the 30 mrad range will be done to check this. For the last three trials, the TLD's were rinsed in acetone before annealing, which seemed to improve the accuracy of TLD #2's corrected readings. Inspection of the uncorrected results shows a striking effect - for the first two trials they read low, as expected, but thereafter, read high. It may be that some silver-containing contamination from the pan also has thermoluminescent properties, and that this contamination is partly absorbed into a TLD during anneal, creating the high response after a few trials. In any event, this effect would occur with all TLD's read, so that a correction based upon the "standard" TLD's would tend to take this into account.

This correction procedure, although greatly increasing the number of TLD's read to make the dose estimates, and requiring individual labeling of the TLD's, gives a means of checking the overall performance of the TLD-reader dosimetry system. It seems that any researcher using such a system should make this type of study at least once, just to see how reproducible his results are. Then, if deemed necessary, this procedure could be used as needed. Based upon Table 3, even uncorrected readings were never more than 10% in error, and this may be an acceptable precision in many applications. Further, silver is more reactive (especially with fluorides) than some other pan materials (e.g., Pt), so other researchers using different phosphors and/or pan materials might not observe these effects.

B. Clinical Applications of Activation Analysis

1. Measurement of Deuterium and Deuterium Labelled Compounds Using the (γ,n) Reaction

One of the more imprtant tracers used in medicine involves the isotopes of hydrogen. Although deuterium is stable and several commercially available detection systems are currently in use, tritium is often the preferred isotope due to the relative ease of its detection. Tritium is radioactive, emitting a low-energy Beta and possessing a half-life of approximately 12.5 years.

We believe that deuterium would be used more routinely by many more institutions if a convenient counting method were available for its detection.

Several groups have suggested the use of the D(γ,n)H reaction as a possible method for the detection of deuterium. We intend to pursue this idea and develop a clinically useful system that will allow its use in routine studies and stimulate further development of Deuterium Tracer Kinetics. This method looks like a particularly promising photo reaction as the threshold energy is very low (2.23 MeV) and therefore one may easily produce this reaction before other photoneutron reactions turn on. Thus, background neutrons should not be a problems.

If one chooses to count the neutrons produced, then the variable parameters are the source detectors and geometry.

We have done some preliminary investigations into these parameters.

A. Sources:

Several sources exist which emit photons of energy greater than the threshold energy. Table 1 lists these with some pertinent characteristics. A bremsstrahling source would appear at first to be the natural source in a hospital environment as many large hospitals possess these type sources in their Radiotherapy Center. However, several disadvantages are apparent.

1. Higher energy linacs activate most everything
2. The useful flux from lower energy clinical linacs is lower than isotopic sources.
3. Although physically nearby, they are not always available in a busy radiotherapy department.
4. It is sometimes difficult to use "borrowed" equipment.

Na-24 would appear an ideal source except for the very short half-life. High activity sources are very easy to produce with a reactor. Therefore it is possible to consider having a facility in the immediate reactor vicinity. This has been proposed by others and we have done some preliminary work along these lines.

Ga-72 is notably more difficult to obtain than Na-24 and also has a short $T_{\frac{1}{2}}$.

Th"C" (from a natural decay series) would be very expensive if not impossible to obtain in the quantities required.

CO-56 would also appear unreasonable at first as it is not reactor produced. However, it may be possible to produce significant size sources caused in the (p,n) reaction on iron near large accelerators, and LAMPF is considering making it available. Having a 77 da half-life it would appear much more attractive than Na-24 although it emits many other γ's besides the useful ones. We are in contact with LASL concerning the possibility of their producting this type source.

B. Detectors:

Our requirements on detection demand high efficiency and low γ-sensitivity. Several type neutron counters are available. Regardless of the type, all high efficiency neutron detectors require that the neutrons first be thermalized (as thermal neutron crossections can be 4-5 orders of magnitude larger than fast neutron crossections). The only reasonable moderator is a hydrogenous material. All other moderators would require so much material as to significantly lower the geometric efficiency. Of course, all hydrogenous moderators will contain deuterium (0.015% natural abundance). This could lead to a large background number of neutrons if the moderator is placed in a large flux high γ-energy field. Solving this problem should also resolve any problem concerning γ-sensitivity of detectors.

We have done some preliminary work with indium foils, and although the efficiency of these foils is very large, due to the inconvenience of having a two step process (activating then counting), we have for the moment discontinued experimenting with them.

The two other most common neutron detectors are BF_3 and He proportional counters. We feel either would be appropriate. Helium counters are more efficient; however, they are more expensive and more γ-noise susceptible. Therefore, we are currently working with BF_3 proportional counters.

C. Current Design Ideas

We are currently of the belief that the best way to obtain a maximum sensitivity facility is to use as large a γ source as may be safely produced and used with the sample positioned next to the source. This would all be in a lead cask of sufficient thickness so as to reduce the γ-flux to a tolerable limit. As the produced neutron flux is being reduced by $1/R^2$ and the γ-flux is being attenuated by both $1/R^2$ and exponentially, by using several counters, we should be able to overcome any loss in geometric efficiency.

D. Preliminary Experiment:

We have conducted a preliminary experiment in collaboration with the Isotopes Technology Division of ORNL. They have modified a lead cask 80 cm in diameter so a large (~200Ci) Na-24 source may be placed in its center and a test tube may be positioned next to it. A BF_3 proportional counter 2" diameter - 12½" Active length) borrowed from the Analytical Chemistry group at ORNL was used on the outside of the cask. A 1-3/4" thick block of paraffin was used as moderator. Positioning of the deuterated water samples was the major source of error leading to uncertainties much larger than statistics. However we were able to determine an approximate sensitivity of 70 cpm/mg of D_2O. We believe that we can improve this by a factor greater than 20 by optimizing moderator thickness, pulse height discrimination and using more detectors. Background counting rates in a neutron free area is ~7 cpm. Therefore, we feel that these sensitivities will allow us to conduct several experiments,

1. We intend to first attempt total body water dilution studies on animals and then people. We expect samples to be in the milligram of D_2O range and therefore straight forward to do.
2. Recent papers have suggested that Deuterium can be used in bile salt metabolism in infants. We will need μg sensitivity here.
3. Possible other studies including Lipid or fatty acid metabolism studies, and kidney function studies might be possible.

Although it is envisioned that a large Na-24 source facility could only be available near a reactor, thereby not being available for emergency studies, this facility would allow routine studies of various nature to be done with little difficulty and excellent sensitivity.

2. Cf-252 Neutron Activation Facility - feasibility study

We are investigating two different techniques to measure bone mineral content. The first, which we now have operational, is the dual isotope transmission scan using 153-Gd. This method allows us to measure the total mineral content (calcium and phosphorous) of the bone. The other technique is in-vivo neutron activation analysis. Using this method, the calcium content of bone can be measured by activating Ca-48 and then counting the γ-rays given off by Ca-49. We propose to use both methods on the forearm to find the calcium-to-total mineral ratio. If a total body transmission scan is also done, the total body calcium content can then be calculated.

We also plan to use the activation facility for in-vitro activation and neutron radiography. Our present design of this facility is shown in Figure 1. We plan to use six 2 mg. sources of Cf-252. Calculations have shown that in order to obtain the maximum thermal neutron flux at the center, the sources are arranged in a ring (radius = 2.5 cm.) and are surrounded by a polyethylene sphere (4.5 cm. radius) which acts as a moderator. This is then surrounded by a 35 cm. radius graphite reflector with lead and borated polyethylene shielding on the outside. The whole facility will be located beneath the floor to provide additional shielding.

A collimator with its inlet at the center of the ring of sources and axis perpendicular to the plane of sources will provide a beam of neutrons which will be used for arm activation and neutron radiography. A tube may be inserted into the collimator for activation of samples in-vitro at the center of the sources where the flux is a maximum and uniform. Additional tubes may be placed around the outside of the ring of sources for long-term sample activation.

We have been investigating the possible use of stable tracers to help diagnose various diseases and monitor their progression. In this method a stable isotope that is not normally found in a biological system is administered and a sample of the biological system is obtained. The sample is then activated and the quantity of the tracer in the sample is measured by counting the γ-rays given off by the sample that are characteristic of the activated tracer. We have performed calculations to determine the amounts of various isotopes we would be able to detect on a sample. The results of these calculations are shown in Table 1.

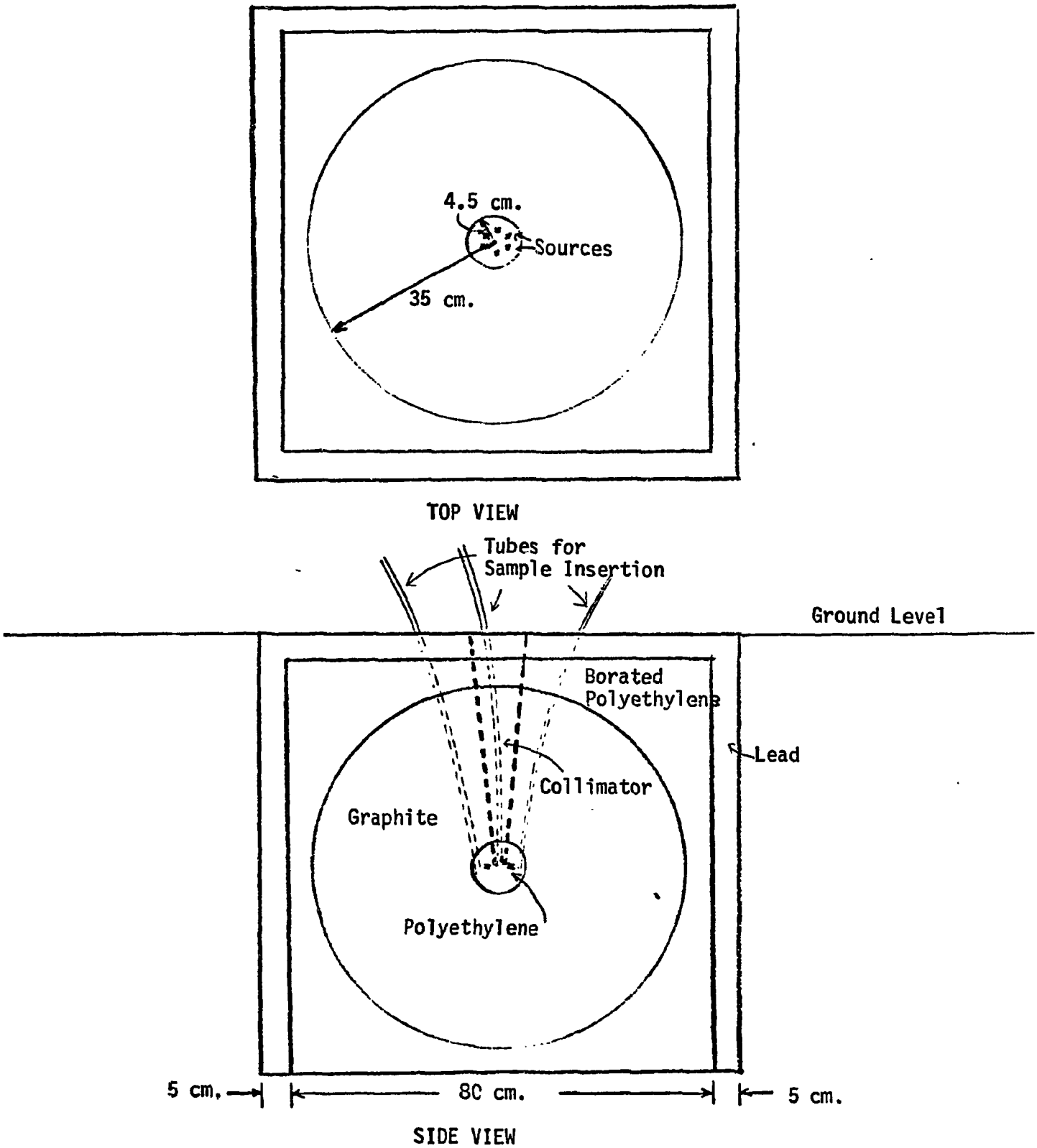

Figure 1 Proposed Cf-252 Neutron Irradiation Facility.

Table 1

Mass of Various Elements that may be Measured In-Vitro with

Proposed Neutron Activation Facility

ISOTOPE[1]	MASS (mg)[2]	ISOTOPE[1]	MASS (mg)[2]
Ne-22	1.0	Ag-107	5.0
Na-23	0.7	Cd-116	0.3
Mg-26	4.0	In-115	0.002
Al-27	3.0	Sn-122	0.3
Si-30	1000.0	Sb-121	1.0
S-36	5.0	Te-130	0.4
Cl-37	0.6	I-127	0.1
Ar-40	0.2	Xe-136	10.0
K-41	4.0	Cs-133	0.3
Ca-48	0.5	Ba-138	0.7
Sc-45	5.0	La-139	0.7
Ti-50	0.7	Ce-142	3.0
V-51	0.1	Pr-141	8.0
Cr-50	7.0	Nd-148	0.09
Mn-55	0.01	Sm-154	0.02
Fe-58	100.0	Eu-151	0.002
Co-59	0.1	Gd-160	0.6
Ni-64	0.3	Tb-159	6.0
Cu-65	2.0	Dy-164	0.003
Zn-70	20.0	Ho-165	0.02
Ga-71	0.2	Er-170	0.08
Ge-74	2.0	Tm-169	30.0
As-75	0.5	Yb-168	0.006
Se-74	3.0	Lu-175	0.08
Br-81	0.8	Hf-178	0.8
Kr-84	1.0	Ta-181	3.0
Rb-87	10.0	W-186	0.3
Sr-86	0.1	Re-187	0.1
Y-87	80.0	Os-189	30.0
Nb-93	200.0	Ir-193	0.1
Mo-100	1.0	Pt-198	0.2
Ru-104	2.0	Au-197	0.05
Rh-103	0.003	Hg-196	0.02
Pd-108	2.0		

[1] If the natural abundance of the isotope if less than 90%, it is assumed that it is enriched to 90%.

[2] Mass that could be detected when irradiated for 1 hour and counted for 1 hour assuming 10,000 counts collected with no interference from other isotopes.

Appendix I. The Linear Pan Correction

The dependence of the observed TLD reading will be assumed to have the general form

$$TL = k_1 D (k_2 + n k_3), \tag{I-1}$$

where

- TL = the observed TLD reading
- D = dose to TLD
- k_1 = the TLD-dependent constant relating the dose and emitted light
- k_2 = the TLD-independent constant which indicates the pan reflectivity at the start of a readout
- k_3 = a TLD-independent constant which indicates the rate at which the reflectivity is changing
- n = an integer showing when the TLD was read (n = 0 for the first one, n = 1 for the second, etc.)

Thus the term in parentheses in (I-1) describes the change in pan reflectivity and is linear in n.

When three "standard" TLD's are read in the "standard" pan, one has

$$R_1 = TL_1 / D = k_{11} k_2 \tag{I-2}$$

$$R_2 = TL_2 / D = k_{12} (k_2 + k_3) \tag{I-3}$$

$$R_3 = TL_3 / D = k_{13} (k_2 + 2 k_3). \tag{I-4}$$

These TLD's are then annealed and dosed again so that a set of TLD's to be read can each be corrected for pan changes. For this readout, one has

$$\bar{R}_1 = k_{11} \bar{k}_2 \tag{I-5}$$

(part of desired TLD set)

$$\bar{R}_2 = k_{12} (\bar{k}_2 + m \bar{k}_3) \tag{I-6}$$

(rest of desired TLD set)

$$\bar{R}_3 = k_{13} (\bar{k}_2 + n \bar{k}_3). \tag{I-7}$$

Equations (I-2) through (I-7) can be solved for the ratios k_3/k_2, $\bar{k}_2/k_2$, and $\bar{k}_3/k_2$ in terms of the known readings.

From (I-2) and (I-5), one immediately has

$$\bar{k}_2 / k_2 = \bar{R}_1 / R_1 . \tag{I-8}$$

From (I-3) and (I-6), one has, using (I-8),

$$\bar{R}_2 / R_2 = \left[\bar{R}_1 / R_1 + m\left(\bar{k}_3 / k_2\right)\right] / \left(1 + k_3 / k_2\right), \tag{I-9}$$

and from (I-4) and (I-7),

$$\bar{R}_3 / R_3 = \left[\bar{R}_1 / R_1 + n\left(\bar{k}_3 / k_2\right)\right] / \left(1 + 2\, k_3 / k_2\right). \tag{I-10}$$

Solving (I-9) and (I-10) for k_3/k_2 and $\bar{k}_3/k_2$ gives

$$k_3 / k_2 = \frac{n(a_2 - a_1) - m(a_3 - a_1)}{2 m a_3 - n a_2} \tag{I-11}$$

$$\bar{k}_3 / k_2 = \frac{a_2(a_1 - a_3) - 2 a_3 (a_1 - a_2)}{2 m a_3 - n a_2} , \tag{I-12}$$

where

$$a_1 = \bar{R}_1 / R_1 , \quad a_2 = \bar{R}_2 / R_2 , \quad \text{and} \quad a_3 = \bar{R}_3 / R_3 .$$

When the experimental values of a_1 (1.0151), a_2 (1.0205), a_3 (0.99095), m(4), and n(5) are used, one obtains

$$k_3 / k_2 = -0.265 , \qquad \bar{k}_3 / k_2 = -0.269 . \tag{I-13}$$

To see how to use these values to correct a reading for pan changes, note that the reading of a TLD in the desired set would be described by

$$TL = k_1 D \left(\bar{k}_2 + l \bar{k}_3 \right), \tag{I-14}$$

since it was read out between equations (I-5) and (I-7). This can be rewritten as

$$TL = k_1 D k_2 \left(\bar{k}_2 / k_2 + l \bar{k}_3 / k_2 \right), \tag{I-15}$$

so that if one divides (I-15) by the term in parentheses, the resulting

expression should be equal to what this TLD would have read under the "standard" pan conditions of the first "standard" TLD. That is, dividing (I-15) by the quantity in parentheses gives the right side the same form as (I-2). Further, the readings from the "standard" TLD's can all be corrected in the same way.

The values in (I-13) are so negative, however, that the quantity in parentheses in (I-15) will be negative whenever $l \geq 5$. For smaller values of l, it becomes so small that the corrections for pan changes are unreasonably large as well. Thus, the assumed form of (I-1) is probably incorrect.

Appendix II

The Method of Activity Determination in Patients

In order to set up the formalism, imagine the scan field to be divided up into a large number of rectangles, or cells, as shown in Figure 1. The length of each cell is equal to the distance moved by the scanner when counts are recorded for one data point, and the width of each cell is equal to the distance between scan lines. When the detectors traverse the length of a cell, the counts accumulated in that time are recorded by a computer, thus giving a data point corresponding to that cell.

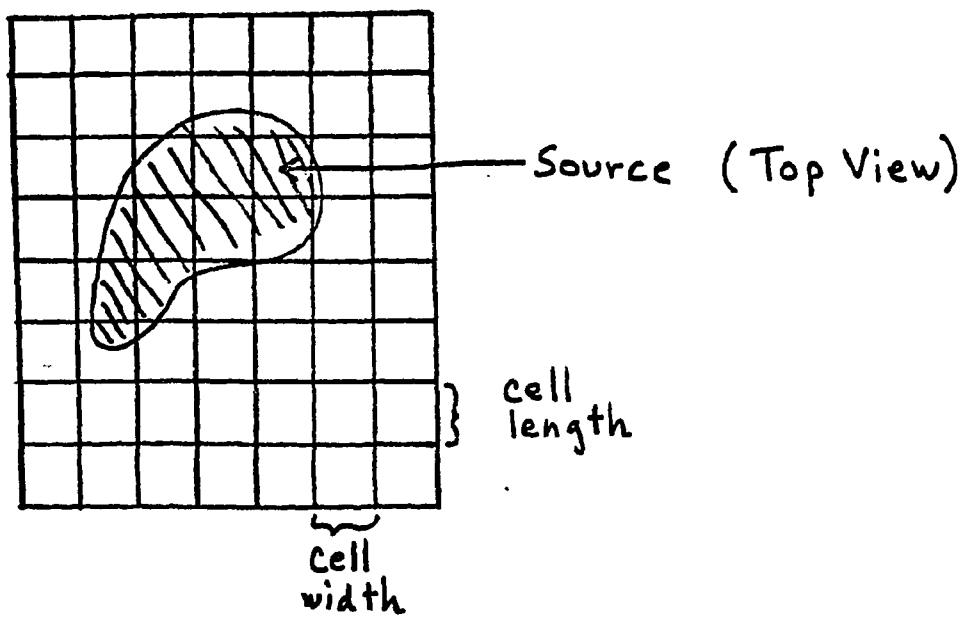

Figure 1. The division of the scan field. The size of the cells is greatly exaggerated for clarity. In this case, there are 56 cells in the scan field. In the usual case, there are 4096.

To calibrate the scanner, a "point" source of known activity is placed in a constant-thickness phantom and scanned. We define

$$S_{ij}(d,z) = \frac{\text{counts recorded in data point } i \text{ due to activity in cell } j}{\text{activity in cell } j} \qquad (1)$$

where d is the phantom thickness and z the height of the source from the bed. In order that this be a well-defined parameter, one must have the cell sizes much smaller than the area of the collimator field of view. Otherwise, the precise x-y location of the "point" source within a given cell would be important.

There would be a calibration factor of the form of (1) for each detector, but wherever possible, an explicit distinction between top and bottom detector functions will not be made, for the sake of brevity.

The calibration function for each detector is

$$f(d,z) = \sum_{i}^{n} S_{ij}(d,z) \tag{2}$$

and there is an $f_T(d,z)$ for the top detector, and $f_B(d,z)$ for the bottom one. Experimentally, these functions are found by summing the counts over the scan image, and dividing by the source activity. These functions were found to have the form

$$f_T(d,z) = a\, e^{-\mu(d-z)} \qquad f_B = f_B(z) = b\, e^{-\mu z} \tag{3}$$

where a, b, and μ are constants. These represent exponential attenuation of the photons being counted (see figure 2).

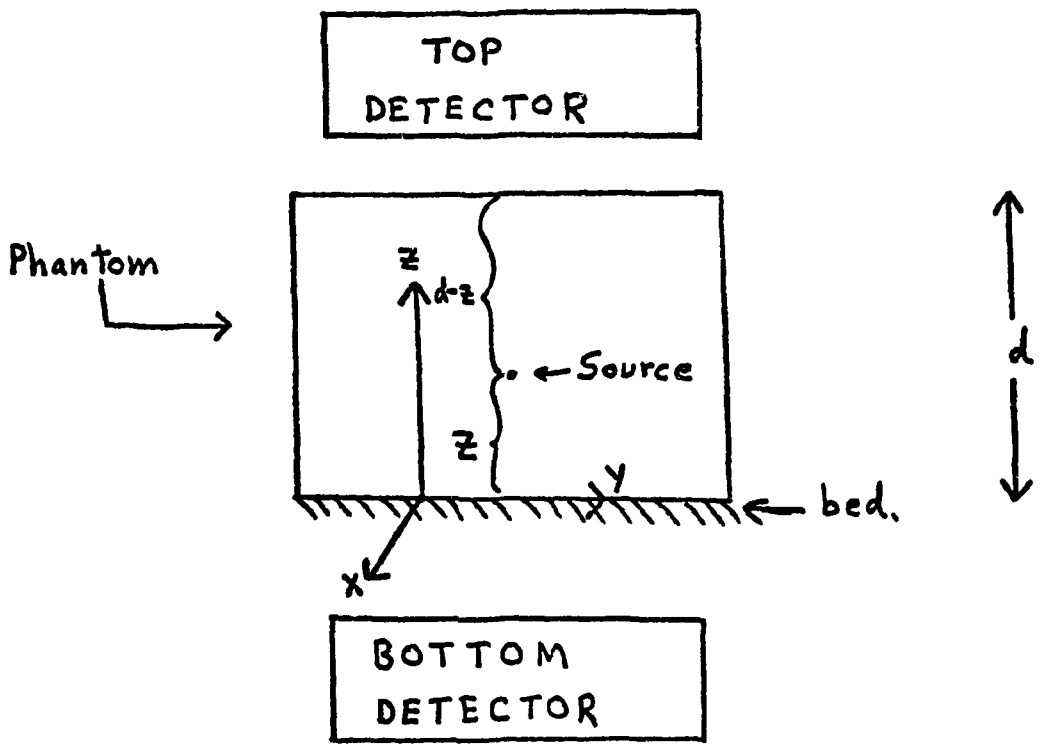

Figure 2. The coordinate system used. A point source at height z in a phantom of thickness d is shown.

Now consider the case of a uniform source of varying thickness located in a phantom of varying thickness. This is assumed to be the case for patients. The uniform source is assumed largely because a better assumption is not known, but it should be adequate, especially for healthy patients.

The counts in data point i due to the activity A_j in cell j is given by

$$C_{ij} = \left(\frac{A_j}{t_j}\right) \int_{z_{j1}}^{z_{j2}} S_{ij}(?, z_j)\, dz_j \tag{4}$$

where t_j is the source thickness in cell j, and the ? means that the correct phantom thickness to use is unknown. In general, this would depend upon all the cell thicknesses, because of Compton scattering, but it is assumed here that d_j (phantom thickness in cell j) is the primary factor. This should be a good approximation because patient thickness does not change much from one cell to another (except along the sides of the trunk, where little or no activity is located), and the exponential form of (3) implies that not too much scatter is being counted anyway. Then (4) becomes

$$C_{ij} = \left(\frac{A_j}{t_j}\right) \int_{z_{j1}}^{z_{j2}} S_{ij}(d_j, z_j)\, dz_j$$

and the total counts in data point i is

$$C_i = \sum_j^m C_{ij} = \sum_j^m \left(\frac{A_j}{t_j}\right) \int_{z_{j1}}^{z_{j2}} S_{ij}(d_j, z_j)\, dz_j \,. \tag{5}$$

In order to write the scan results in terms of the calibration function given by (2), we must sum (5) over the image of the source:

$$C = \sum_i^l C_i = \sum_j^m \left(\frac{A_j}{t_j}\right) \int_{z_{j1}}^{z_{j2}} \sum_i^l S_{ij}(d_j, z_j)\, dz_j \tag{6}$$

or

$$C = \sum_j^m \left(\frac{A_j}{t_j}\right) \int_{z_{j1}}^{z_{j2}} f(d_j, z_j)\, dz_j \tag{7}$$

where the fact that l>n does not matter because the S_{ij} which make the major contribution to (6) are the same S_{ij} which appear in (2). Substituting (3) into (7) gives

$$C_T = a \sum_j^m A_j e^{\mu z_{j1}} e^{\mu t_j/2} \frac{\sinh(\mu t_j/2)}{(\mu t_j/2)} e^{-\mu d_j} \tag{8}$$

$$C_B = b \sum_j^m A_j e^{-\mu z_{j1}} e^{-\mu t_j/2} \frac{\sinh(\mu t_j/2)}{(\mu t_j/2)} \tag{9}$$

for the top and bottom detectors, respectively. The apparent activity $\bar{A}$ is given by

$$\bar{A} = (C_T C_B)^{1/2} \Big/ \left[f_T(d, z_0)\, f_B(d, z_0) \right]^{1/2} \tag{10}$$

where z_0 is a dummy variable (the denominator of (10) is independent of it with the functions in (3)), and d is some sort of average phantom thickness to be specified. Using (8), (9), and (3), (10) becomes

$$\bar{A} = \frac{\left[\sum_j^m A_j e^{\mu z_{j1}} e^{\mu t_j/2} \frac{\sinh(\mu t_j/2)}{(\mu t_j/2)} e^{-\mu d_j} \sum_j^m A_j e^{-\mu z_{j1}} e^{-\mu t_j/2} \frac{\sinh(\mu t_j/2)}{(\mu t_j/2)} \right]^{1/2}}{e^{-\mu d/2}} \tag{11}$$

This equation is hard to evaluate, because the t_j and d_j are uncorrelated (they are measured with different instruments), and because the z_{j1} are difficult to find even with an ultrasonic scan. However, this equation can be reduced with the Schwarz Inequality:

$$\sum_j^m X_j^2 \sum_j^m Y_j^2 = \left(\sum_j^m X_j Y_j \right)^2, \text{ if } \frac{Y_j}{X_j} \text{ is independent of } j \tag{12a}$$

$$\sum_j^m X_j^2 \sum_j^m Y_j^2 > \left(\sum_j^m X_j Y_j \right)^2, \quad \text{otherwise.} \tag{12b}$$

With the definitions

$$X_j^2 = A_j e^{\mu z_{j1}} e^{\mu t_j/2} \frac{\sinh(\mu t_j/2)}{(\mu t_j/2)} e^{-\mu d_j}$$

$$Y_j^2 = A_j e^{-\mu z_{j1}} e^{-\mu t_j/2} \frac{\sinh(\mu t_j/2)}{(\mu t_j/2)},$$

(11) and (12) give

$$\bar{A} = e^{\mu d/2} \sum_j^m A_j \frac{\sinh(\mu t_j/2)}{(\mu t_j/2)} e^{-\mu d_j/2}, \quad \text{if } e^{-\mu d_j} e^{2\mu z_{j1}} e^{\mu t_j} \text{ is independent of } j \tag{13a}$$

$$\bar{A} > e^{\mu d/2} \sum_j^m A_j \frac{\sinh(\mu t_j/2)}{(\mu t_j/2)} e^{-\mu d_j/2}, \quad \text{otherwise.} \tag{13b}$$

This can be written in terms of the total source activity, since the source is uniform:

$$A_j / t_j = A / \sum_j^m t_j, \qquad \left(A = \sum_j^m A_j \right)$$

which implies that

$$\bar{A}/A = e^{\mu d/2} \sum_j^m e^{-\mu d_j/2} \left(\frac{t_j}{\sum_j t_j} \right) \frac{\sinh(\mu t_j/2)}{(\mu t_j/2)}, \quad \text{if the same ratio is independent of } j \tag{14a}$$

$$\bar{A}/A > e^{\mu d/2} \sum_j^m e^{-\mu d_j/2} \left(\frac{t_j}{\sum_j^m t_j} \right) \frac{\sinh(\mu t_j/2)}{(\mu t_j/2)}, \quad \text{otherwise.} \tag{14b}$$

Unfortunately, (14a) is also hard to evaluate, again because the d_j and t_j are not correlated. However, d remains to be picked as well, and we will see that the proper choice of d will lead to an accurate approximation to (14a). To see what this choice is, consider the special case in which all the t_j are the same. For that, (14a) would be

$$\bar{A}/A = e^{\mu d/2} \left(\frac{1}{m} \sum_j^m e^{-\mu d_j/2} \right) \frac{\sinh(\mu t/2)}{(\mu t/2)},$$

which will reduce to the self-attenuation correction (the last term) if d is chosen so that

$$e^{-\mu d/2} = \frac{1}{m} \sum_j^m e^{-\mu d_j/2}. \tag{15}$$

This expression for d will be used for the source of varying thickness as well.

To obtain a suitable approximate expression from (14a), the exponentials are combined and expanded in a power series:

$$\bar{A}/A = \sum_j^m \left(\frac{t_j}{\sum_j^m t_j}\right) \frac{\sinh(\mu t_j/2)}{(\mu t_j/2)} - \frac{\mu d}{2} \sum_j^m \left(\frac{d_j}{d}-1\right)\left(\frac{t_j}{\sum_j^m t_j}\right) \frac{\sinh(\mu t_j/2)}{(\mu t_j/2)}$$

$$+ \left(\frac{\mu d}{2}\right)^2 \frac{1}{2!} \sum_j^m \left(\frac{d_j}{d}-1\right)^2\left(\frac{t_j}{\sum_j^m t_j}\right) \frac{\sinh(\mu t_j/2)}{(\mu t_j/2)} - \left(\frac{\mu d}{2}\right)^3 \frac{1}{3!} \tag{16}$$

$$\sum_j^m \left(\frac{d_j}{d}-1\right)^3\left(\frac{t_j}{\sum_j^m t_j}\right) \frac{\sinh(\mu t_j/2)}{(\mu t_j/2)} + \left(\frac{\mu d}{2}\right)^4 \frac{1}{4!} \sum_j^m \left(\frac{d_j}{d}-1\right)^4\left(\frac{t_j}{\sum_j^m t_j}\right) \frac{\sinh(\mu t_j/2)}{(\mu t_j/2)} - \cdots$$

The first term is easily evaluated with ultrasonic data, but the other terms still require correlated ultrasonic and transmission scan data. The approximation, then, is to ignore these other terms, and replace the entire series by the first term only. To see if this is valid, first note that all the values of $\sinh(\mu t_j/2)(\mu t_j/2)$ will be in range from 1.0 - 1.3 for the values of μt to be encountered here, so to within an order of magnitude, and maybe even better, this series becomes

$$\bar{A}/A \sim \frac{\sinh(\mu t/2)}{(\mu t/2)} \left[1 - \frac{\mu d}{2} \frac{1}{m} \sum_j^m \left(\frac{d_j}{d}-1\right) + \left(\frac{\mu d}{2}\right)^2 \frac{1}{2!} \frac{1}{m} \cdot \right. \tag{17}$$

$$\left. \sum_j^m \left(\frac{d_j}{d}-1\right)^2 - \left(\frac{\mu d}{2}\right)^3 \frac{1}{3!} \frac{1}{m} \sum_j^m \left(\frac{d_j}{d}-1\right)^3 + \left(\frac{\mu d}{2}\right)^4 \frac{1}{4!} \frac{1}{m} \sum_j^m \left(\frac{d_j}{d}-1\right)^4 - \cdots \right],$$

where $\sinh(\mu t/2)/(\mu t/2)$ is an average of the individual values of this function. Each of the terms in brackets was computed for each patient study done thus far, and gave results similar to those in Table 1.

Table 1.

Computer calculations of the terms in (14) from transmission scan data of patients.

d = 9.83"

First Sum = 0.015 = $\frac{1}{m} \sum_j^m \left(\frac{d_j}{d}-1\right)$

Second Sum = 0.025 = $\frac{1}{m} \sum_j^m \left(\frac{d_j}{d}-1\right)^2$

Third Sum = 0.00114 = $\frac{1}{m} \sum_j^m \left(\frac{d_j}{d}-1\right)^3$

Fourth Sum = 0.00161 = $\frac{1}{m} \sum_j^m \left(\frac{d_j}{d}-1\right)^4$

For this value of d, $\mu d = 3$, so that (17) becomes

$$\bar{A}/A \sim \frac{\sinh(\mu t/2)}{(\mu t/2)} \left[1 - \frac{3}{2}(.015) + \frac{9}{8}(.025) - \frac{27}{48}(.00114) + \frac{81}{16\cdot 24}(.00161) - \ldots\right]$$

$$\bar{A}/A \sim \frac{\sinh(\mu t/2)}{(\mu t/2)} \left[1 - .0225 + .0281 - .000641 + .000340 - \ldots\right]$$

$$\bar{A}/A \sim \frac{\sinh(\mu t/2)}{(\mu t/2)} \left[1 + .0056 - .000301 - \ldots\right].$$

Evidently, this is a very good approximation, because the term after the 1 is about two orders of magnitude less. This was surprising, since the standard deviation of these d_j values is about 15.4% of their average. To check this, another calculation was done with the same data, only

$$\bar{d} = (1/m) \sum_j^m d_j$$

was used in place of d. This gave

$$\bar{A}/A \sim \frac{\sinh(\mu t/2)}{(\mu t/2)} \left[1 - 0 + \frac{9}{8}(.0237) - \frac{27}{48}(.000025) - \frac{81}{16\cdot 24}(.00149) - \ldots\right]$$

$$\bar{A}/A \sim \frac{\sinh(\mu t/2)}{(\mu t/2)} \left[1 + .0267 - .0000127 + .000315 - \ldots\right],$$

indicating a somewhat larger, but still acceptable error in truncating the series. More importantly, the value of d given by (15) has the advantage of being somewhat less than $\bar{d}$, so that the first two sums in (17) tend to cancel each other. With $\bar{d}$ the first sum is zero, so this does not happen. Thus, d picked by (15) is a better value to use than $\bar{d}$, because of this cancellation effect.

Therefore, if (14a) is valid, it can be evaluated to a good approximation by the expression.

$$\bar{A}/A = \sum_j^m \left(\frac{t_j}{\sum_j^m t_j}\right) \frac{\sinh(\mu t_j/2)}{(\mu t_j/2)},$$

where d is picked from (15). But if (14a) is not valid, the value of A computed in this way will be an upper limit to the true activity, as can be seen from (14b). Consequently, we turn our attention to the validity of (14a).

The condition which must be met is

$$e^{-\mu d_j} e^{+2\mu z_{j1}} e^{\mu t_j} = K,$$

where K is independent of j. This is equivalent to the condition

$$d_j - 2z_{j1} - t_j = k, \qquad \left(k = -\frac{1}{\mu} \ln K \right)$$

or (18)

$$d_j - (z_{j1} + z_{j2}) = k.$$

To interpret this equation physically, imagine that the cells are so small that d_j, z_{j1}, and z_{j2} can be expressed as functions of the position variables x and y, i.e., the cells are infinitesimal. Then $d_j = d(x,y)$, and similarly for z_{j1} and z_{j2}, so that (18) has the form

$$d(x,y) - \left(z_1(x,y) + z_2(x,y) \right) = k.$$

Defining $z_0(x,y)$ as the average of z_1 and z_2, this equation can be written in the differential form

$$d\left[d(x,y) \right] - 2\, d\left[z_0(x,y) \right] = 0,$$

where d [ ] means the differential of the quantity in brackets. Using the chain rule, this becomes

$$\frac{\partial d(x,y)}{\partial x} dx + \frac{\partial d(x,y)}{\partial y} dy - 2 \frac{\partial z_0(x,y)}{\partial x} dx - 2 \frac{\partial z_0(x,y)}{\partial y} dy = 0$$

$$\left(\frac{\partial d(x,y)}{\partial x} - 2 \frac{\partial z_0(x,y)}{\partial x} \right) dx + \left(\frac{\partial d(x,y)}{\partial y} - 2 \frac{\partial z_0(x,y)}{\partial y} \right) dy = 0$$

$$\underline{\nabla} \left(d(x,y) - 2 z_0(x,y) \right) \cdot d\underline{r} = 0,$$

where $\underline{\nabla}$ is the gradient operator, and $d\,\underline{r} = dx\hat{i} + dy\hat{j}$. This last equation states that the directional derivative of the phantom thickness must equal twice that of the source midpoint, for a given direction in the x-y plane and given set of (x,y) values. Further, this must be true over the entire extent of the source. This condition is probably not exactly true for patients, although large organs (such as the liver) may tend to follow the general body shape. So it is important to see how sensitive (14a) is to this condition being met.

This has been investigated as well. The method of investigation is to first examine the Schwarz Inequality in a general way, and then make a specific examination with the functions in (11) and (12). The first examination is fairly simple, and will be shown here, while the other is more involved, so only an outline of it will be given.

First, suppose that the condition for equality is violated by only a small amount. That is,

$$x_j = c\,y_j + \epsilon_j$$

where c is a constant, and ϵ_j represents the violation of each term. Then

$$\sum_j^m x_j^2 \sum_j^m y_j^2 = \sum_j^m (c\,y_j + \epsilon_j)^2 \sum_j^m y_j^2 =$$

$$\left(c^2 \sum_j^m y_j^2 + 2c \sum_j^m y_j \epsilon_j + \sum_j^m \epsilon_j^2\right) \sum_j^m y_j^2 \approx \tag{19}$$

$$c^2 \left(\sum_j^m y_j^2\right)^2 + 2c \sum_j^m y_j \epsilon_j \sum_j^m y_j^2 ,$$

where the last step follows because ϵ_j^2 will be negligible. This represents the left side of either (12a) or (12b). The right side is simply

$$\left(\sum_j^m x_j y_j\right)^2 = \left(\sum_j^m (c\,y_j + \epsilon_j)\, y_j\right)^2 = \left(\sum_j^m c\,y_j^2 + \sum_j^m \epsilon_j y_j\right)^2$$

$$= c^2\left(\sum_j^m y_j^2\right)^2 + 2c \sum_j^m y_j^2 \sum_j^m \epsilon_j y_j + \left(\sum_j^m \epsilon_j y_j\right)^2 \tag{20}$$

$$\approx c^2 \left(\sum_j^m y_j^2\right)^2 + 2c \sum_j^m \epsilon_j y_j \sum_j^m y_j^2 .$$

Comparing the last step of (19) to that of (20) shows them to be equal. So to first order in ε_j, the Schwarz Inequality is still an equality. This is an important result, because it means that even if the condition for (14a) is not exactly met, (14a) is still valid, i.e., the Schwarz Inequality is not very sensitive to this condition. This gives hope that (14a) may be adequate for patient estimates.

If one does not neglect the ε_j^2 terms of (19) and (20), there results the condition

$$\sum_j^m Y_j^2 \sum_j^m \epsilon_j^2 \geq \left(\sum_j^m Y_j \epsilon_j\right)^2, \tag{21}$$

where the equality holds if (14a) is true, and the > holds otherwise. For the functions in (11),

$$X_j^2 = A_j\, e^{-\mu d_j}\, e^{\mu t_j/2}\, e^{\mu z_{j1}} \frac{\sinh(\mu t_j/2)}{(\mu t_j/2)}$$

$$Y_j^2 = A_j\, e^{-\mu t_j/2}\, e^{-\mu z_{j1}} \frac{\sinh(\mu t_j/2)}{(\mu t_j/2)},$$

from which $\epsilon_j = X_j - c\,Y_j$ can be found, and hence ε_j^2. Substituting these expressions into (21) finally results in

$$\left(\sum_j^m A_j\, e^{-\mu t_j/2}\, e^{-\mu z_{j1}} \frac{\sinh(\mu t_j/2)}{(\mu t_j/2)}\right)\left(\sum_j^m A_j\, e^{-\mu d_j}\, e^{\mu t_j/2}\, e^{\mu z_{j1}} \frac{\sinh(\mu t_j/2)}{(\mu t_j/2)}\right) \geq \left(\sum_j^m A_j\, e^{-\mu d_j/2} \frac{\sinh(\mu t_j/2)}{(\mu t_j/2)}\right)^2. \tag{22}$$

At this point, use is made of (18), giving it the form

$$d_j - 2z_{j1} - t_j = k + \delta_j$$

where δ_j is the violation corresponding to ε_j. Solving this for z_{j1} and

substituting into (22) finally gives

$$\left(\sum_j^m A_j e^{-\mu d_j/2} e^{\mu \delta_j/2} \frac{\sinh(\mu t_j/2)}{(\mu t_j/2)} \right) \left(\sum_j^m A_j e^{-\mu d_j/2} e^{-\mu \delta_j/2} \frac{\sinh(\mu t_j/2)}{(\mu t_j/2)} \right) \geq \left(\sum_j^m A_j e^{-\mu d_j/2} \frac{\sinh(\mu t_j/2)}{(\mu t_j/2)} \right)^2 .$$

By using the definitions of the sinh and cosh functions, the $\exp(\mu \delta_j/2)$ and $\exp(-\mu \delta_j/2)$ can be eliminated to give

$$\left(\sum_j^m A_j e^{-\mu d_j/2} \frac{\sinh(\mu t_j/2)}{(\mu t_j/2)} \cosh(\mu \delta_j/2) \right)^2 - \left(\sum_j^m A_j e^{-\mu d_j/2} \frac{\sinh(\mu t_j/2)}{(\mu t_j/2)} \sinh(\mu \delta_j/2) \right)^2 \geq \left(\sum_j^m A_j e^{-\mu d_j/2} \frac{\sinh(\mu t_j/2)}{(\mu t_j/2)} \right)^2 \tag{23}$$

This is still not in the desired form. Each term on the left side of (23) can be reduced by applying the Schwarz Inequality:

$$\left(\sum_j^m A_j e^{-\mu d_j/2} \frac{\sinh(\mu t_j/2)}{(\mu t_j/2)} \cosh(\mu \delta_j/2) \right)^2 \leq \sum_j^m A_j^2 e^{-\mu d_j} \left(\frac{\sinh(\mu t_j/2)}{(\mu t_j/2)} \right)^2 \sum_j^m \cosh^2(\mu \delta_j/2)$$

$$\left(\sum_j^m A_j e^{-\mu d_j/2} \frac{\sinh(\mu t_j/2)}{(\mu t_j/2)} \sinh(\mu \delta_j/2) \right)^2 \leq \sum_j^m A_j^2 e^{-\mu d_j} \left(\frac{\sinh(\mu t_j/2)}{(\mu t_j/2)} \right)^2 \sum_j^m \sinh^2(\mu \delta_j/2).$$

Because the left side of (23) is a difference of two terms, substituting these expressions into it would lead to ambiguity, in general. However, we will make these substitutions anyway, and then show that this procedure is actually correct.

Making this substitution gives

$$\sum_j^m A_j^2 e^{-\mu d_j} \left(\frac{\sinh(\mu t_j/2)}{(\mu t_j/2)} \right)^2 \left[\sum_j^m \cosh^2(\mu \delta_j/2) - \sum_j^m \sinh^2(\mu \delta_j/2) \right]$$
$$\overset{?}{\geq} \left(\sum_j^m A_j e^{-\mu d_j/2} \frac{\sinh(\mu t_j/2)}{(\mu t_j/2)} \right)^2, \tag{24}$$

where the ? indicates the ambiguity.
The quantity in brackets is just equal to m, the number of terms in the sum, because of a well-known identity of the cosh and sinh functions. So, dividing both sides of (24) by m^2 gives

$$\frac{1}{m} \sum_j^m A_j^2 e^{-\mu d_j} \left(\frac{\sinh(\mu t_j/2)}{(\mu t_j/2)} \right)^2 \overset{?}{\geq} \left(\frac{1}{m} \sum_j^m A_j e^{-\mu d_j/2} \frac{\sinh(\mu t_j/2)}{(\mu t_j/2)} \right)^2. \tag{25}$$

For simplicity, make the definition

$$E_j \equiv A_j e^{-\mu d_j/2} \frac{\sinh(\mu t_j/2)}{(\mu t_j/2)},$$

so that (25) is

$$\frac{1}{m} \sum_j^m E_j^2 \overset{?}{\geq} \left(\frac{1}{m} \sum_j^m E_j \right)^2. \tag{26}$$

Regarding the E_j values as a statistical set of numbers, the variance of this set would be given by

$$\sigma^2 = \frac{1}{m} \sum_j^m E_j^2 - \left(\frac{1}{m} \sum_j^m E_j \right)^2,$$

and is a positive definite quantity. Thus, in (26), the left side is truly greater than the right, so that the ? can be removed. Continuing on back, it can also be removed from (25) and (24), showing that the substitution made into (23) is actually correct; there is <u>no</u> ambiguity.

Equation (25), without the ?, is the equation to be analyzed further. Removing A_j in favor of A, as was done with (13a), multiplying both sides by $e^{\mu d}$ and taking the square root gives

$$\left[\frac{1}{m} A^2 \sum_j^m \left(\frac{t_j}{\sum_j t_j} e^{-\mu(d_j-d)/2} \frac{\sinh(\mu t_j/2)}{(\mu t_j/2)}\right)^2\right]^{1/2} \geq \frac{1}{m} A \sum_j^m \frac{t_j}{\sum_j t_j} e^{-\mu(d_j-d)/2} \frac{\sinh(\mu t_j/2)}{(\mu t_j/2)}$$

$$\left[\frac{1}{m} \sum_j^m \left(\frac{t_j}{\sum_j t_j} e^{-\mu(d_j-d)/2} \frac{\sinh(\mu t_j/2)}{(\mu t_j/2)}\right)^2\right]^{1/2} \geq \frac{1}{m} \sum_j^m \frac{t_j}{\sum_j t_j} e^{-\mu(d_j-d)/2} \frac{\sinh(\mu t_j/2)}{(\mu t_j/2)}. \quad (27)$$

The right side of this expression is just the right side of (14a), which, as was shown in (17), can be evaluated accurately by replacing the exponentials by 1. This will also be true of the left side, since it has practically the same form. So, the same patient data as before can be used to test the irequality above, in exactly the same way that (17) was used to test the approximation of (14a). One has, to within an order of magnitude (possibly better):

$$\frac{\sinh(\mu t/2)}{(\mu t/2)} \left[1 - .0450 + .0562 - .001282 + .000680\right]^{1/2} \gtrsim$$

$$\frac{\sinh(\mu t/2)}{(\mu t/2)} \left[1 - .0225 + .0281 - .000641 + .000340\right],$$

or

$$(1 + .0112 - .00060)^{1/2} \gtrsim 1 + .0056 - .000301$$

$$\sqrt{1.0106} \gtrsim 1.0053,$$

and these two numbers are practically equal. This, and equation (27) are extremely important results, because they mean that when one is checking the approximate method of evaluation of (14a), he is also checking on the validity of (14a) as compared to the validity of (11). If the approximate method of evaluating (14a) is seen to be adequate, then (14a) is a good approximation to (11). If the approximate method gives a poor result, then (14a) is about an equally poor approximation to (11), and one must decide upon other methods to evaluate (11), or use a different method of activity determination.

C. APPENDIX III: Publications

No.		AEC Report No.
1.	Greenlaw, R.H., Weinstein, M.B., Brill, A.B., McBain, J.K., Murphy, L., and Kniseley, R.M. Gallium-67 citrate imaging in untreated malignant lymphoma. Preliminary Report of Cooperative Group. Oak Ridge, Tennessee. J Nuc Med 15: 404-407, 1974.	73
2.	Scott, H.W., Dean, R.H., Shull, H.J., Gluck, F., Abram, H.S., Webb, W., Younger, R.K., and Brill, A.B. Jejunoileal bypass for morbid obesity: A presentation of results in 100 patients. J Tn Med Assoc 67: 203, 1974.	74
3.	Ivancevic, D., Price, R.R., Rhea, T., Graham, T.P., Atwood, G.F., and Brill, A.B. Computer analysis of radiocardiograms of patients with intracardiac shunts. Proceedings of IAEA Symposium on Dynamic Studies with Radioisotopes in Clinical Medicine and Research, Knoxville, Tennessee (1974), IAEA-SM-185/28.	75
4.	Brill, A.B., Parker, J.F., Erickson, J.J., Price, R.R., and Patton, J.A. CAMAC applications in nuclear medicine at Vanderbilt: present status and future plans. IEEE Trans Nuclear Science, NS 21, No. 1., 892-898, 1974.	76
5.	Brill, A.B., Page, D., Dyer, N., and Baglan, R. Neutron activation analysis and atomic absorption analysis of 18 elements in relation to a study of tracer elements in cardiovascular diseases. IAEA-157. Trace Elements in Relation to Cardiovascular Diseases. Technical Report published by IAEA, Vienna, 1973.	77
6.	Price, R.R., McKee, L.C., Jr., Krantz, S.B., and Brill, A.B. Estimation of slow dynamic function parameters in iron kinetics studies using quantitative measurements and compartmental modelling analysis. Proceedings IAEA Symposium on Dynamic Studies with Radioisotope in Clinical Medicine Research. 1974. IAEA-SM-185/38.	78
7.	Price, R.R., Johannes, J.D., Lutin, C.D., Krolak, P.D., and Brill, A.B. Computer-aided nuclear medicine report generation at Vanderbilt. AEC - CONF - 740531. 18-31.	79
8.	Erickson, J., Brill, A.B., Patton, D.D., Williams, H., Ahuja, S., and Price, R.R. Automated brain bolus analyses and significances of various extracted parameters. AEC - CONF 740531. 51-69, 1974.	80

9. Patton, J.A., Brill, A.B. and Hollifield, J.W. Thyroid Uptake and Iodine Content Via Computer. Fourth Symposium on Sharing of Computer Programs and Technology in Nuclear Medicine. (USAEC CONF, 1974) 128-139. 81

10. Patton, D.D., McKee, P., and Patton, J.A. Separation of Osteoblastic from vascular activity on bone scans by dual isotope technique. Proceedings of the First World Congress of Nuclear Medicine. World Federation of Nuclear Medicine and Biology. (1974) 959-960. 82

11. Brill, A.B., Parker, J.F., Erickson, J.J., Price, R.R., and Patton, J.A. CAMAC applications in nuclear medicine at Vanderbilt: present status and future. Proceedings of the First World Congress of Nuclear Medicine, World Federation of Nuclear Medicine and Biology. (1974) 144-145. 83

Abstracts:

12. Price, R.R., Patton, J.A., and Brill, A.B. Regional and whole-body bone mineral content measurement with a rectilinear scanner. Southern Med J 67 (October 1974).

13. Patton, J.A., Versage, P., Blei, L., Price, R., Patton, D., and Brill, A.B. Report on the status of thyroid data bases at Vanderbilt. Fifth Symposium on Sharing of Computer Programs and Technology in Nuclear Medicine. 1975 (In press).

14. Ivancevic, D., Price, R.R., Rhea, T.C., Graham, T.P., Smith, C.V. Accuracy of cardiac shunt estimates for radiocardiographic measurements and computer analyses using a pulsatile flow model. J Nuc Med 15: 504, 1974.

15. Rhea, T.C., Ivancevic, D., Price, R.R., Graham, T.P., Smith, C.V., and Brill, S.B., Pulse: a computer code incorporating a pulsatile heart model to analyze radiocardiographic data. J Nuc Med 15: 527, 1974.

16. Rhea, T.C., Graham, T.P., Nelson, J.H., Iida, H., Price, R.R., Lindstrom, D., and Brill, A.B. Ventricular volume determinations "on-line" using a video/computer system. Circulation 50 (in press).

17. Price, R.R., Lindstron, D.P., Hillis, S., Friesinger, G.C., and Brill, A.B. Analytical techniques for image superposition. Proceeding of Fifth Symposium on Sharing of Computer Programs and Technology in Nuclear Medicine. Salt Lake City, Utah January 1975 (in press).

18. Erickson, J.J., Versage, P., Brill, A.B., In-vitro test programming at Vanderbilt. Proceedings of Fifth Symposium on Sharing of Computer Programs and Technology in Nuclear Medicine. Salt Lake City, Utah. January 1975 (in press).

C. APPENDIX III: Publications

No.		AEC Report No.
1.	Greenlaw, R.H., Weinstein, M.B., Brill, A.B., McBain, J.K., Murphy, L., and Kniseley, R.M. Gallium-67 citrate imaging in untreated malignant lymphoma. Preliminary Report of Cooperative Group. Oak Ridge, Tennessee. J Nuc Med 15: 404-407, 1974.	73
2.	Scott, H.W., Dean, R.H., Shull, H.J., Gluck, F., Abram, H.S., Webb, W., Younger, R.K., and Brill, A.B. Jejunoileal bypass for morbid obesity: A presentation of results in 100 patients. J Tn Med Assoc 67: 203, 1974.	74
3.	Ivancevic, D., Price, R.R., Rhea, T., Graham, T.P., Atwood, G.F., and Brill, A.B. Computer analysis of radiocardiograms of patients with intracardiac shunts. Proceedings of IAEA Symposium on Dynamic Studies with Radioisotopes in Clinical Medicine and Research, Knoxville, Tennessee (1974), IAEA-SM-185/28.	75
4.	Brill, A.B., Parker, J.F., Erickson, J.J., Price, R.R., and Patton, J.A. CAMAC applications in nuclear medicine at Vanderbilt: present status and future plans. IEEE Trans Nuclear Science, NS 21, No. 1., 892-898, 1974.	76
5.	Brill, A.B., Page, D., Dyer, N., and Baglan, R. Neutron activation analysis and atomic absorption analysis of 18 elements in relation to a study of tracer elements in cardiovascular diseases. IAEA-157. Trace Elements in Relation to Cardiovascular Diseases. Technical Report published by IAEA, Vienna, 1973.	77
6.	Price, R.R., McKee, L.C., Jr., Krantz, S.B., and Brill, A.B. Estimation of slow dynamic function parameters in iron kinetics studies using quantitative measurements and compartmental modelling analysis. Proceedings IAEA Symposium on Dynamic Studies with Radioisotope in Clinical Medicine Research. 1974. IAEA-SM-185/38.	78
7.	Price, R.R., Johannes, J.D., Lutin, C.D., Krolak, P.D., and Brill, A.B. Computer-aided nuclear medicine report generation at Vanderbilt. AEC - CONF - 740531. 18-31.	79
8.	Erickson, J., Brill, A.B., Patton, D.D., Williams, H., Ahuja, S., and Price, R.R. Automated brain bolus analyses and significances of various extracted parameters. AEC - CONF 740531. 51-69, 1974.	80

2869

MAY 1 1975

9. Patton, J.A., Brill, A.B. and Hollifield, J.W. Thyroid Uptake and Iodine Content Via Computer. Fourth Symposium on Sharing of Computer Programs and Technology in Nuclear Medicine. (USAEC CONF, 1974) 128-139. 81

10. Patton, D.D., McKee, P., and Patton, J.A. Separation of Osteoblastic from vascular activity on bone scans by dual isotope technique. Proceedings of the First World Congress of Nuclear Medicine. World Federation of Nuclear Medicine and Biology. (1974) 959-960. 82

11. Brill, A.B., Parker, J.F., Erickson, J.J., Price, R.R., and Patton, J.A. CAMAC applications in nuclear medicine at Vanderbilt: present status and future. Proceedings of the First World Congress of Nuclear Medicine, World Federation of Nuclear Medicine and Biology. (1974) 144-145. 83

Abstracts:

12. Price, R.R., Patton, J.A., and Brill, A.B. Regional and whole-body bone mineral content measurement with a rectilinear scanner. Southern Med J 67 (October 1974).

13. Patton, J.A., Versage, P., Blei, L., Price, R., Patton, D., and Brill, A.B. Report on the status of thyroid data bases at Vanderbilt. Fifth Symposium on Sharing of Computer Programs and Technology in Nuclear Medicine. 1975 (In press).

14. Ivancevic, D., Price, R.R., Rhea, T.C., Graham, T.P., Smith, C.V. Accuracy of cardiac shunt estimates for radiocardiographic measurements and computer analyses using a pulsatile flow model. J Nuc Med 15: 504, 1974.

15. Rhea, T.C., Ivancevic, D., Price, R.R., Graham, T.P., Smith, C.V., and Brill, S.B., Pulse: a computer code incorporating a pulsatile heart model to analyze radiocardiographic data. J Nuc Med 15: 527, 1974.

16. Rhea, T.C., Graham, T.P., Nelson, J.H., Iida, H., Price, R.R., Lindstrom, D., and Brill, A.B. Ventricular volume determinations "on-line" using a video/computer system. Circulation 50 (in press).

17. Price, R.R., Lindstron, D.P., Hillis, S., Friesinger, G.C., and Brill, A.B. Analytical techniques for image superposition. Proceeding of Fifth Symposium on Sharing of Computer Programs and Technology in Nuclear Medicine. Salt Lake City, Utah January 1975 (in press).

18. Erickson, J.J., Versage, P., Brill, A.B., In-vitro test programming at Vanderbilt. Proceedings of Fifth Symposium on Sharing of Computer Programs and Technology in Nuclear Medicine. Salt Lake City, Utah. January 1975 (in press).